This article has been accepted for publication in IEEE Open Journal of the Communications Society. This is the author's version which has not been fully edited and content may change prior to final publication. Citation information: DOI 10.1109/OJCOMS.2023.3341621

IEEE Open Journal of the Communications Society

Received XX Month, XXXX; revised XX Month, XXXX; accepted XX Month, XXXX; Date of publication XX Month, XXXX; date of current version XX Month, XXXX.

Digital Object Identifier 10.1109/OJCOMS.2022.1234567

Accurate phase synchronization for Precoding-enabled GEO multibeam satellite systems

LIZ MARTÍNEZ MARRERO*, ***Member, IEEE***, **JUAN MERLANO DUNCAN***, ***Senior Member, IEEE***, **JORGE LUIS GONZÁLEZ***, ***Member, IEEE***, **JEVGENIJ KRIVOCHIZA***, ***Member, IEEE***, **SYMEON CHATZINOTAS***, ***Fellow Member, IEEE***, **BJÖRN OTTERSTEN***, ***Fellow Member, IEEE*** **and, ADRIANO CAMPS**†, ***Fellow Member, IEEE***

[1]SnT, University of Luxembourg, 29, avenue JF Kennedy, L-1855 Luxembourg
[2]Universitat Politècnica de Catalunya, Barcelona, Spain
[3]Institut d'Estudis Espacials de Catalunya, Barcelona, Spain

CORRESPONDING AUTHOR: Liz Martínez Marrero (e-mail: liz.martinez-marrero@uni.lu).

This research was funded by the Luxembourg National Research Fund (FNR) under the CORE project COHESAT: Cognitive Cohesive Networks of Distributed Units for Active and Passive Space Applications, grant reference [FNR11689919] and the project DISBuS: Dynamic Beam Forming and In-band Signalling for Next Generation Satellite Systems, grant reference [FNR13778945]. For the purpose of open access, the author has applied a Creative Commons Attribution 4.0 International (CCBY4.0) license to any Author Accepted Manuscript version arising from this submission. Additionally, this work has been supported by the European Space Agency under project number 4000122451/18/NL/NR "Live Satellite Precoding Demonstration - CCN: MEO case (LiveSatPreDem)." (Opinions, interpretations, recommendations, and conclusions presented in this paper are those of the authors and are not necessarily endorsed by the European Space Agency).

ABSTRACT Synchronizing the local oscillators in multibeam satellites with the objective of coherent communications is still an open challenge. It has to be addressed to implement full-frequency reuse approaches, such as precoding techniques using the already deployed multibeam satellites. This article addresses the required phase synchronization to enable precoding techniques in multibeam satellite systems. It contains the detailed design of a frequency and phase compensation loop based on the proportional-integral controller, which deals with the phase drift introduced by the hardware components. Specifically, the phase noise of the local oscillators used for up and down conversion at each system element (gateway, satellite, and user terminals). The implementation of the two-state phase noise model used to emulate this phase drift is included in the article. Besides, a comparative analysis of several methods to combine the frequency and phase measurements obtained from the user terminals is also included. Finally, the performance of the proposed closed-loop synchronization method is validated through simulations using our in-house developed MIMO end-to-end satellite emulator based on SDR platforms.

INDEX TERMS geosynchronous orbit, multi-beam satellite, phase noise, phase synchronization, precoding, software-defined radio.

I. INTRODUCTION

MULTIBEAM high throughput satellites are the primary providers for meeting the broadband needs of remote regions [1]. Realizing their full potential relies on advanced technologies such as precoding implementations [2]–[4]. Precoding is a signal processing technique to mitigate interference and enhance system performance. In multiple-input and multiple-output (MIMO) systems, precoding algorithms calculate the optimal transmission weights for the antennas at the transmitter, considering the channel conditions, interference, and system constraints [5], [6]. These weights are then applied to the data symbols before transmitting them over the wireless channel. By using precoding, the transmitted signals can be tailored to exploit the channel characteristics, such as reducing the impact of interference and fading and improving the overall spectral efficiency of the system [2]. However, because it involves manipulating the transmitted signal phase, its effectiveness depends on the accurate synchronization of the clock references, i.e., local oscillators (LOs) across all beams. Unless this issue

This work is licensed under a Creative Commons Attribution 4.0 License. For more information, see https://creativecommons.org/licenses/by/4.0/

This work is licensed under a Creative Commons Attribution 4.0 License. For more information, see https://creativecommons.org/licenses/by/4.0/

This article has been accepted for publication in IEEE Open Journal of the Communications Society. This is the author's version which has not been fully edited and content may change prior to final publication. Citation information: DOI 10.1109/OJCOMS.2023.3341621

is addressed, none of the widely studied and proposed approaches in non-terrestrial networks [2], [7], [8] would be feasible.

Most synchronization algorithms reported in the literature for distributed MIMO systems rely on inter-satellite links [9]–[11]. However, this approach is not feasible in multi-beam satellite systems. While using a common LO as a clock reference may seem like a potential solution, it is not a practical alternative in satellite systems. This limitation arises from various technical constraints, including independence between payloads, autonomy, robustness, prevention of cross-interference between radio frequency (RF) channels, and the incorporation of redundancy, as outlined in [12]. Additionally, the work in [13] formally demonstrated that even when a common clock reference is used at the transponder, the Doppler effect and the oscillator's phase noise degrade the system performance.

Practical implementations of precoding-enabled satellite systems must address the phase drift introduced by different system components, such as the phase noise introduced by the LOs used for up and down conversion at each system element (gateway (GW), satellite, and user terminals (UTs)). The phase noise is an inherent characteristic of the oscillators, and it can be attributed to factors such as aging, thermal noise, mechanical vibrations, and more. This phenomenon means that the output of an oscillator is not limited to a single spectral line at the nominal frequency; instead, it exhibits side-band power, leading to phase and frequency instabilities, as noted in Rutman's work [14]. However, in many cases, oscillators are assumed to be ideal during the precoding design process. For instance, [15] and [16] proposed the design and performance analysis of precoding-enabled satellite systems considering the time-varying phase noise introduced by onboard satellite oscillators. Both studies modeled the phase uncertainty as a Gaussian random process with a mean of zero and a standard deviation within the range of 2°to 20°. Another example can be found in Mubarak Umar Aminu's work [17], where the authors investigated the effects of non-ideal oscillators in a multi-antenna hybrid digital-analog beamforming transceiver architecture. Through simulations, they determined that the system performance is more affected when the phase noise is modeled as a Wiener process rather than a Gaussian process.

In practice, oscillator noise is influenced by various other phenomena not considered in the above-mentioned models. Many researchers have delved into this topic, aiming to develop advanced models for characterizing oscillator near-carrier power spectral density (PSD) [18], [19]. One such model, the Two-state Phase Noise Model proposed by Galleani in [20], accounts for the frequency deviation of a cesium clock using two components: a white noise and a Wiener process. The latter is responsible for the random walk nature of the frequency deviation, while the white noise represents the local oscillations. This model balances complexity and rigor, making it a suitable choice. Consequently, we have chosen the two-state phase noise model to emulate the phase noise in our system, thus validating our synchronization algorithm design.

During precoding operations, the differential phase errors product of the phase noise are perceived by the UT as part of the channel state information (CSI), which the precoding matrix will compensate for. However, the variation rate of this differential phase error is faster than CSI estimation loop frequency, implying that the compensation applied by the precoding matrix is insufficient, thus degrading the system performance [13]. To solve this problem, we propose a phase synchronization loop with a faster response than the typical precoding loop. Our design estimates and compensates for the phase error between beams in a sample-based mode. Meanwhile, the precoding matrix is calculated and applied by groups of symbols or frames following a conventional precoding implementation.

Additionally, we compare several methods for combining the differential phase estimations between beams. Given that all the UTs report the differential phase between beams, while the compensation loop requires a single measurement as input, we have examined four approaches to address this problem effectively. In this context, some authors have highlighted the advantages of the weighted average algorithm over the equal gain combining method [21], [22]. Nevertheless, the effectiveness of the weighted average algorithm depends on the careful selection of weights for each estimation [21], [22].

Combining estimations from different sensors also presents challenges in cognitive radio systems engaged in cooperative spectrum sensing [23], [24]. Despite some similarities between this scenario and satellite communication systems, a key distinction preventing the direct application of cooperative spectrum sensing methods is that, in the former case, decision fusion involves a binary problem—detecting the presence or absence of the primary user. Meanwhile, in the scenario discussed in this paper, our objective is to combine different angle measurements, which can assume any value within the interval $(-\pi, \pi)$. While other methods proposed for multi-sensor data fusion, such as the evidence theory [25], fuzzy theory [26], Z-number [27], and D-number [28], [29], do consider the combination of angle measurements, they tend to be more complex due to their objective of combining different types of data. For this reason, we have incorporated the well-known Weighted Average algorithm and three selective approaches named the Basic, the Best Receiver, and the Best Estimation approaches. These choices were made to strike a balance between effectiveness and complexity in addressing the input requirements of our phase synchronization loop.

Unlike cooperative spectrum sensing in cognitive radio and multi-sensor data fusion, the problem of phase combining in precoding-enabled satellite systems remains largely unexplored. This is primarily due to the relative novelty of precoding-enabled satellites; all practical demonstrations

This work is licensed under a Creative Commons Attribution 4.0 License. For more information, see https://creativecommons.org/licenses/by/4.0/

This article has been accepted for publication in IEEE Open Journal of the Communications Society. This is the author's version which has not been fully edited and content may change prior to final publication. Citation information: DOI 10.1109/OJCOMS.2023.3341621

thus far have involved only a single receiver [30], [31]. We propose incorporating some simple and well-known combinatorial approaches to address this gap. For instance, using the sensor's signal-to-noise ratio (SNR) as a decision fusion metric has shown promise in cooperative spectrum sensing [32], [33]. In addition to this metric, we consider each beam's received power and explore various combination approaches.

Precoding techniques have been employed in commercial wireless networks for several years, starting from the 802.11n Wi-Fi standard [34]. However, there are only a few field trials of precoding-enabled satellite systems [30], [31]. Both examples [30], [31] considered two transmitters and two receivers and synchronization algorithms based on phase-locked loops (PLLs). In [30], the frequency synchronization is guaranteed using a digital PLL with 7 Hz bandwidth. According to the theoretical analysis presented in [30], the system could achieve 5° of phase uncertainty after compensation by using their solution. Meanwhile, the over-the-air demonstration in [31] used a frequency and phase tracking and compensation loop implemented in the GW. The article demonstrates how this compensation effectively stabilizes frequency and phase drift. However, it is important to note that none of the previously mentioned articles provide an in-depth analysis of the synchronization algorithm's design or its impact on the system's performance. The present article addresses this gap by comprehensively explaining the synchronization algorithm employed in [31]. Additionally, we analyze the impact of the synchronization on the system performance.

In brief, this article presents the design of the phase synchronization method required to enable the precoding implementations in the geostationary orbit (GEO) scenario. The proposed solution requires only small modifications to the already deployed satellite systems. The only modification with respect to traditional precoding design is including a controller at the GW. As a further step in the validation of the proposed solution, we performed experiments over an FPGA-based system emulator. This approach enables us to achieve a more realistic approximation to the actual precoding-enabled satellite system scenario without incurring the expenses associated with conducting over-the-air tests. For instance, this method helps us address challenges such as the return link variable delay, which are often overlooked in traditional Matlab simulations.

Summarizing, the main contributions of this article are:

- Modeling the phase drift introduced by the LOs in a multi-beam satellite as a two-state clock model.
- The design of the closed-loop phase synchronization method from a practical implementation point of view, considering the phase drift introduced by the hardware components.
- The analysis of different approaches for using the phase estimation reported by the UTs in combinatorial and selective algorithms.
- The hardware implementation of the closed-loop phase synchronization and the combinatorial phase estimation algorithms.
- The experimental real-time validation of the proposed solution using the in-house developed MIMO end-to-end satellite emulator based on software-defined radio (SDR) platforms.

The rest of this article is organized as follows: section II describes the system model. Meanwhile, section III details the design of the proposed phase synchronization method. The hardware implementation is described in section IV. Section V contains the validation of the proposed solution using the MIMO end-to-end satellite emulator, and section VI concludes the article.

A. LIST OF ACRONYMS

CFO	carrier frequency offset
ChEm	channel emulator
CSI	channel state information
DVB-S2X	extension of the Digital Video Broadcasting - Satellite second generation
FLL	frequency-locked loop
FM	frequency modulated
GEO	geostationary orbit
GW	gateway
IF	intermediate frequency
LO	local oscillator
MAE	mean absolute error
MIMO	multiple-input and multiple-output
MMSE	minimum mean square error
NCO	numerically-controlled oscillator
PI	proportional-integral
PLL	phase-locked loop
PSD	power spectral density
SDR	software-defined radio
SNIR	signal-to-noise-plus-interference ratio
UT	user terminal
USRP	universal software radio peripherals

II. SYSTEM MODEL

We consider a GEO satellite generating N beams towards $K \leq N$ single-antenna UTs as represented in Fig. 1. We collect in $\boldsymbol{h}_i \in \mathbb{C}^{N\times 1}$ the complex (i.e., magnitude and phase) coefficients of the frequency-flat slow fading channels between the beams generated at the GW and the i-th UT. At a given symbol period, independent data symbols $\{s_i : 1 \leq i \leq K\}$ are to be transmitted to the UTs, where s_i denotes the symbol intended for the i-th user. Under the above assumptions, the received vector containing the symbol-sampled complex baseband signals of all K UTs can be modeled as

$$\boldsymbol{r} = \boldsymbol{H}\boldsymbol{W}\boldsymbol{s} + \boldsymbol{z}, \tag{1}$$

where $\boldsymbol{H} = [\boldsymbol{h}_1 \cdots \boldsymbol{h}_K]^T$ denotes the $K \times N$ complex-valued channel matrix, $\boldsymbol{W}$ stands for the $N \times K$ precoding

This work is licensed under a Creative Commons Attribution 4.0 License. For more information, see https://creativecommons.org/licenses/by/4.0/

This article has been accepted for publication in IEEE Open Journal of the Communications Society. This is the author's version which has not been fully edited and content may change prior to final publication. Citation information: DOI 10.1109/OJCOMS.2023.3341621

matrix, $\boldsymbol{s} = [s_1 \cdots s_K]^T$ is a $K \times 1$ complex-valued vector containing the UTs' intended modulated symbols, and $\boldsymbol{z}$ collects independent additive noise components at the UTs' receivers, which are circularly symmetric complex Gaussian random variables with zero mean and variance $\sigma^2 = k_{\mathrm{B}} T_e B$, where k_{B} is the Boltzmann's constant, T_e is the equivalent noise temperature at the input of the receiver [35], and B is the UT bandwidth.

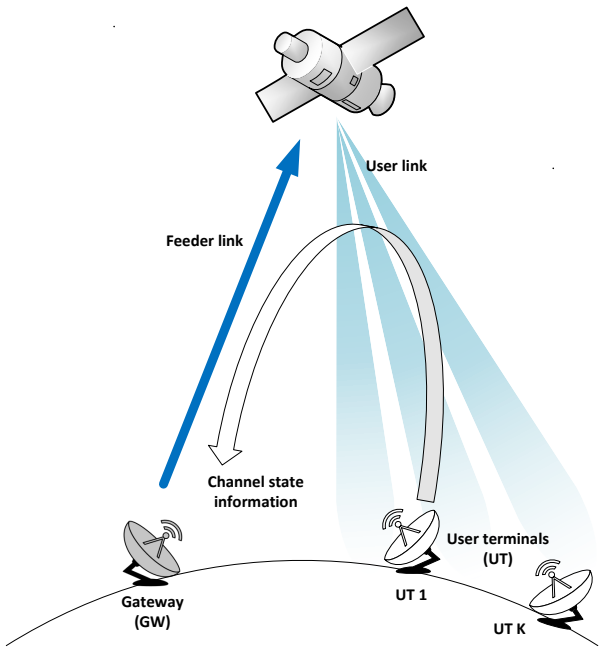

FIGURE 1. System model

The UTs estimate the channel amplitude and phase using the non-precoded pilots periodically transmitted by the GW. The non-precoded pilots contain octogonal Walsh-Hadamard sequences that allows to the UTs to estimate the channel response for each of the received beams. This CSI is sent to the GW where it is used to calculate the precoding matrix $\boldsymbol{W}$ using linear or symbol-level precoding techniques. The experimental results included in Section V were obtained using the linear precoding method minimum mean square error (MMSE). However, the synchronization algorithm proposed in this article is also suitable for symbol-level precoding techniques.

The actual channel matrix can be written as

$$\boldsymbol{H} = \begin{bmatrix} |h_{11}|\mathrm{e}^{j\psi_{11}} & \cdots & |h_{1N}|\mathrm{e}^{j\psi_{1N}} \\ |h_{21}|\mathrm{e}^{j\psi_{21}} & \cdots & |h_{2N}|\mathrm{e}^{j\psi_{2N}} \\ \vdots & \ddots & \vdots \\ |h_{K1}|\mathrm{e}^{j\psi_{K1}} & \cdots & |h_{KN}|\mathrm{e}^{j\psi_{KN}} \end{bmatrix}, \tag{2}$$

where $h_{i,j} = |h_{i,j}|\mathrm{e}^{j\psi_{i,j}}$ denotes the channel coefficient between the i-th UT and the j-th generated beam in the transmit antenna, for any $i \in \{1, 2, ..., K\}$ and $j \in \{1, 2, ..., N\}$, and $|h_{i,j}|$ and $\psi_{i,j}$ respectively represent its magnitude and phase.

However, we have to include a time-varying matrix $\boldsymbol{\Phi}(t)$ to represent the estimated channel matrix available at the GW after collecting the measurements from all the K UTs. $\boldsymbol{\Phi}(t) \triangleq \mathrm{diag}(e^{j\phi_1(t)}, e^{j\phi_2(t)}, ..., e^{j\phi_N(t)})$ accounts for each beam phase drift due to the hardware impairments described in [13]. It was formally demonstrated in [13] that precoding techniques performance is only affected by the phase errors in the uplink channel. The phase noise of the UTs' LOs doesn't impact precoding performance [8]. As a result, $\boldsymbol{\Phi}(t)$ only includes the phase drift in the uplink channel, which is caused by the phase noise of the transponder's LOs. The complete channel matrix can then be written as

$$\hat{\boldsymbol{H}}(t) = \boldsymbol{H}\boldsymbol{\Phi}(t). \tag{3}$$

The following section shows a more detailed description of the model used to emulate $\boldsymbol{\Phi}(t)$.

A. TWO-STATE PHASE NOISE MODEL

The output voltage $u_0(t)$ of a generic oscillator with nominal frequency f_0 is

$$u_0(t) = [A + a(t)]\cos[2\pi f_0 t + \phi(t)], \tag{4}$$

where A is the mean amplitude of the oscillator output, $a(t)$ is the zero-mean amplitude noise and $\phi(t)$ is an error term due to the LO phase noise. We consider that the effects of amplitude noise are overshadowed by the effects of phase noise, which is a common assumption in published work in this field [19], [20].

From (4), we can obtain two fundamental quantities used to characterize clocks: phase and frequency deviation. The frequency deviation $y(t)$, is defined as the derivative of the phase deviation $x(t) = \frac{\phi(t)}{2\pi f_0}$:

$$y(t) = \frac{\mathrm{d}x(t)}{\mathrm{d}t}. \tag{5}$$

Numerous measurements have shown that the continuous phase noise PSD $S_\phi(f)$ tends to be well approximated by a sum of power-law processes

$$S_\phi(f) = \begin{cases} \sum_{\alpha=-4}^{0} h_\alpha f^\alpha & 0 < f < f_h \\ 0 & f \geq f_h \end{cases}, \tag{6}$$

where f_h is the high-frequency cut-off of an infinitely sharp low-pass filter [18]. These $h_\alpha f^\alpha$ terms are related to random walk frequency modulated (FM), flicker FM, white FM, flicker, and white phase noise, respectively [36].

As described in [37], the output phase noise combines contributions from the reference oscillator and a PLL synthesizer. At offset frequencies above 10 kHz, the noise power is dominated by the PLL synthesizer's voltage-controlled oscillator (VCO) phase noise as well as spurs due to digital-to-analog converter (DAC) quantization noise and nonlinearities. For synchronization purposes, we are concerned with oscillator drift at time scales larger or equal to 100 μs, which is determined by noise power at offset frequencies below

This work is licensed under a Creative Commons Attribution 4.0 License. For more information, see https://creativecommons.org/licenses/by/4.0/

This article has been accepted for publication in IEEE Open Journal of the Communications Society. This is the author's version which has not been fully edited and content may change prior to final publication. Citation information: DOI 10.1109/OJCOMS.2023.3341621

10 kHz. At this frequency range, performance is dominated by the reference oscillator and shows two regions: white FM phase noise ($\alpha = 2$) and random walk FM phase noise ($\alpha = 4$) [19]. This is known as the two-state phase noise model.

Experimental evidence confirms that the frequency deviation of a cesium clock is made by the white noise and Wiener process [19]. The last one is responsible for the random walk nature of the frequency deviation, while the white noise accounts for the local oscillations. Therefore, the frequency deviation can be written as

$$y(t) = \xi_1(t) + \int_0^t \xi_2(\dot{t})\mathrm{d}\dot{t}, \tag{7}$$

where $\xi_1(t)$ and $\xi_2(t)$ are two independent zero-mean Gaussian random processes with variance q_1 and q_2 respectively. The term $\int_0^t \xi_2(\dot{t})\mathrm{d}\dot{t}$ represents a Wiener process resultant from the integration of the $\xi_2(t) \backsim \mathcal{N}(0, q_2)$.

To obtain the two-state model of the phase noise, we substitute (5) in (7) and we integrate both sides

$$x(t) = \int_0^t \left(\xi_1(\ddot{t}) + \int_0^{\ddot{t}} \xi_2(\dot{t})\mathrm{d}\dot{t} \right) \mathrm{d}\ddot{t}. \tag{8}$$

Equation (8), shown in graphical form in Fig. 2, describes the two-state phase noise model [19].

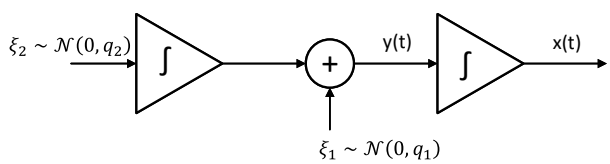

FIGURE 2. Two-state clock noise model

According to [38], q_1 and q_2 are directly related to the Allan variance $\sigma_y^2(\tau)$ through

$$\sigma_y^2(\tau) = \frac{q_1}{\tau} + \frac{q_2 \tau}{3}. \tag{9}$$

This is a typical tool used to characterize the noise in oscillators and could be obtained from experimental measurements. Besides, the IEEE Standard Definitions of Physical Quantities for Fundamental Frequency and Time Metrology [36] relates the Allan variance to the noise PSD in (6) by

$$\begin{aligned}\sigma_y^2(\tau) = h_{-4}\frac{2\pi^2}{3}\tau + h_{-3}2\ln 2 + h_{-2}\frac{1}{2\tau} \\ + h_{-1}\frac{1.038 + 3\ln(2\pi f_h \tau)}{4\pi^2\tau^2} + h_0\frac{3f_h}{4\pi^2\tau^2}.\end{aligned} \tag{10}$$

For the two-state model implemented in this paper, we only consider the first and the third terms in (10). Then, equalling (9) and (10) we obtain

$$\begin{aligned} q_1 &= \frac{h_{-2}}{2} \\ q_2 &= 2\pi^2 h_{-4}. \end{aligned} \tag{11}$$

Using these equations, we can emulate the phase noise for any real or theoretical phase noise PSD. For instance, Fig. 3 shows the PSD of the phase noise emulated with the Two-state model using $h_{-2} = 1.25 \times 10^{-4}$ and $h_{-4} = 0.49$. The target phase noise mask -75 dBc @ 10 Hz is also represented in the figure for comparison. As can be appreciated, the PSD obtained with the emulator is very similar to the target one. Besides, the model output has both slopes: -40 dB/dec and -20 dB/dec, corresponding to f^{-4} and f^{-2} terms in (6) and it is -72.81 dBc/Hz at 10 Hz which is very close to the expected value -75 dBc/Hz. With these points in mind, we can conclude that our implementation of the two-state clock model is accurate, and it can be used to emulate the impairments in our simulations.

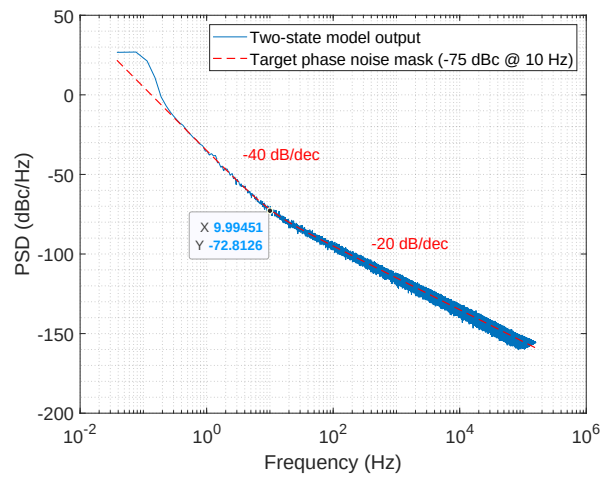

FIGURE 3. Estimated PSD of the phase noise samples generated with the Two-state model

Besides, Fig. 4 shows 20 realizations with a duration of one second. As the figure suggests, the two-state phase noise behavior is smoother than that of a simple Wiener process since it contains a Wiener process plus an integrated Wiener process. This is confirmed by Fig. 5, which represents the mean and variance of the realizations shown in Fig. 4. As can be appreciated, the variance grows quadratically with time, while the variance of a Wiener process increases linearly.

III. DIFFERENTIAL PHASE COMPENSATION LOOP

The proposed closed-loop phase synchronization method is depicted in Fig. 6, where only phase and frequency variables are represented. In the figure, $\boldsymbol{\phi}[k] = \begin{bmatrix}\phi_1[k] & \phi_2[k] & \dots & \phi_N[k]\end{bmatrix}^{\mathrm{T}}$ is an $N \times 1$ vector containing the phase drift of each beam. We define k as the discrete-time variable such that $t[k] = kT_s$ with sampling time T_s. The objective of our design is to pre-compensate

This work is licensed under a Creative Commons Attribution 4.0 License. For more information, see https://creativecommons.org/licenses/by/4.0/

This article has been accepted for publication in IEEE Open Journal of the Communications Society. This is the author's version which has not been fully edited and content may change prior to final publication. Citation information: DOI 10.1109/OJCOMS.2023.3341621

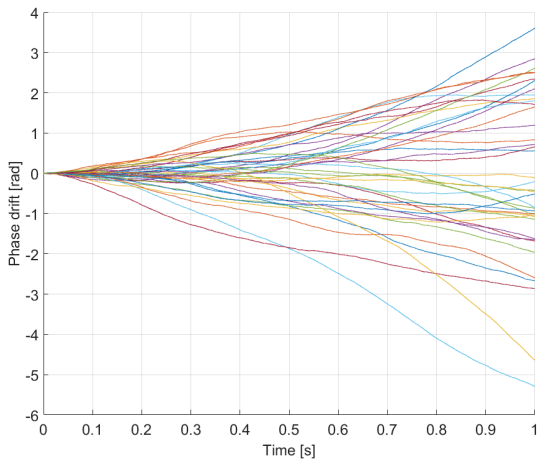

FIGURE 4. Two-state model's output. Some realizations of the phase noise random process

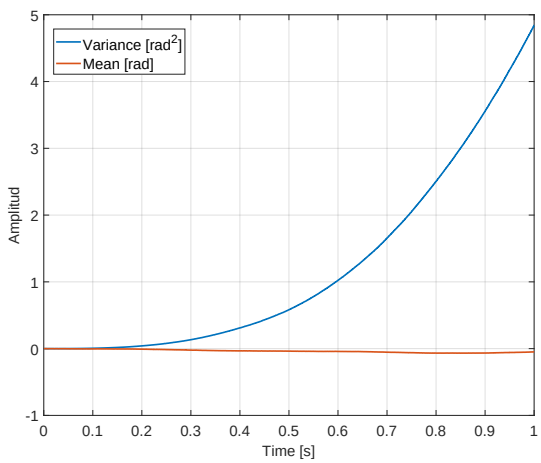

FIGURE 5. Mean and variance of the realizations represented in Fig. 4

the superframe data streams to minimize the value of $\boldsymbol{\phi_e}[k] = \boldsymbol{\phi}[k] - \boldsymbol{\phi_c}[k]$ towards zero. From now on, we will refer to $\boldsymbol{\phi_e}[k]$ as the phase error. The variable $\boldsymbol{\phi_c}[k] = \begin{bmatrix}\phi_1^c[k] & \phi_2^c[k] & \dots & \phi_N^c[k]\end{bmatrix}^{\mathrm{T}}$ is an $N\times 1$ vector representing the phase of the transmitted beams after compensation. The input $\boldsymbol{\Psi}$ represents the phase rotation introduced by the channel matrix $\boldsymbol{H}$.

The vector $\boldsymbol{\theta}[k] = \begin{bmatrix}\theta_1[k] & \theta_2[k] & \dots & \theta_K[k]\end{bmatrix}^{\mathrm{T}}$ in Fig. 6 is a $K \times 1$ vector representing the phase of the received signals at the UTs. The objective of the CSI Estimation block at the UTs is to estimate the attenuation and phase rotation introduced by the channel for each beam using the non-precoded pilots. In a formal notation, the CSI estimated by the kth UT can be represented as a $1 \times N$ complex-valued vector $\hat{\boldsymbol{h}}_i[k] = \begin{bmatrix}\hat{h}_{i1}[k] & \hat{h}_{i2}[k] & \dots & \hat{h}_{iN}[k]\end{bmatrix}$ where each element $\hat{h}_{ij}[k] = |\hat{h}_{ij}[k]|\mathrm{e}^{j(\hat{\theta}_{ij}[k])}, \quad j \in \{1, 2, ..., N\}$. Note that $\hat{\theta}_{ij}[k]$ are relative phase measurements of the jth beam with respect to the intended beam i. These relative phase estimations are the only measurements in practical precoding implementations, as stated in [13]. In a mathematical notation, $\hat{\theta}_{ij}[k] = \psi_{ij}[k] + \phi_j^e[k] - \psi_{ii}[k] - \phi_i^e[k]$, where $\psi_{ij}[k] + \phi_j^e[k]$ and $\psi_{ii}[k] + \phi_i^e[k]$ are the respective absolute phases of the jth and the ith beams received at the ith UT. Besides, it is essential to note that $\hat{\theta}_{ij}[k]$ contains the differential phase rotation introduced by the channel $(\psi_{ij} - \psi_{ii})$ but also the differential phase drift experienced for the beam $(\phi_j^e[k] - \phi_i^e[k])$. However, it is not possible to measure each of them independently. Additionally, we calculate the carrier frequency offset between beams $\hat{\boldsymbol{f}}[k]$ at each UT to use it in the compensation loop. This operation is represented as the derivative block in Fig. 6. $\hat{\boldsymbol{f}}[k]$ is a $K \times 1$ vector with elements

$$\hat{f}_j[k] = \left(\hat{\theta}_j[k] - \hat{\theta}_j[k-1]\right)/2\pi T_s. \tag{12}$$

At the GW, the CSI estimation from all the UTs is grouped in a $K \times N$ complex-valued matrix $\hat{\boldsymbol{H}}[k] = \begin{bmatrix}\hat{\boldsymbol{h}}_1[k] & \hat{\boldsymbol{h}}_2[k] & \dots & \hat{\boldsymbol{h}}_K[k]\end{bmatrix}^{\mathrm{T}}$ which is used to calculate the precoding matrix $\boldsymbol{W}$ in (1). For a given set of UTs, the precoding matrix is not calculated continuously but rather at sufficient intervals to capture the very slow temporal variations of the channel matrix. On the other hand, the compensation loop can operate in a sample-based mode, calculating a compensation phase from each transmitted non-precoded pilot. Our solution was designed as a two-step algorithm that uses the carrier frequency offset at the 'coarse' synchronization step and the differential phase at the 'fine' synchronization step.

Unlike the precoding matrix calculation, which relies on CSI from all the UTs, the compensation loop's input requires the phase difference between beams that can be estimated without requiring measurements from every UT. Consequently, we designed the 'Combine Estimates' block to merge estimations from all the UTs and generate the inputs for the compensation loop. In simpler terms, this block utilizes either a $K \times N$ matrix, $\boldsymbol{F}[k]$ for the 'coarse' step or $\boldsymbol{\Theta}[k]$ for the 'fine' step, to produce a $N \times 1$ vector, $\boldsymbol{f}[k]$ for the 'coarse' step or $\boldsymbol{\theta}[k]$ for the 'fine' step. Within this block, the algorithm selects the reference beam (RB), whose frequency and phase act as a reference and remain uncompensated. Further details regarding the design of this block will be discussed in section B.

The core of our solution is to calculate a compensation phase vector using the combined estimates vectors previously described. This operation is done by the $N-1$ proportional-integral (PI) Controllers represented in Fig. 6. The design of this block is addressed in section A.

The numerically-controlled oscillator (NCO) blocks are fed with $f_{ctrl}[k]$ during the first or 'coarse' synchronization state. This allows shorter lock times. When the differential frequency between beams $f_n[k]$ decreases below a predefined threshold γ, the algorithm starts feeding the NCOs

This work is licensed under a Creative Commons Attribution 4.0 License. For more information, see https://creativecommons.org/licenses/by/4.0/

This article has been accepted for publication in IEEE Open Journal of the Communications Society. This is the author's version which has not been fully edited and content may change prior to final publication. Citation information: DOI 10.1109/OJCOMS.2023.3341621

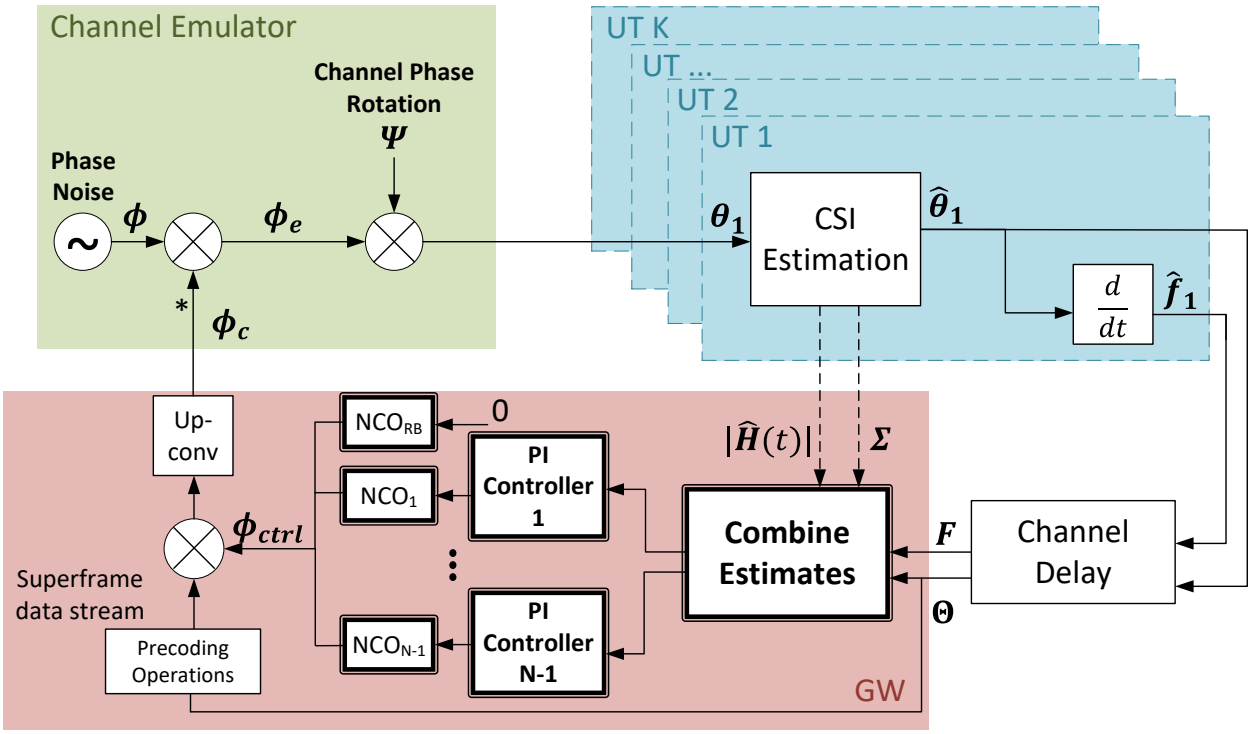

FIGURE 6. **Differential phase-error compensation loop. In the diagram, the highlighted blocks—NCO, PI Controller, and Combine Estimates—are the only modifications necessary to implement this solution in a precoding-enabled multibeam satellite system.**

with $\theta_{ctrl}[k]$. We refer to this state as the 'fine' synchronization step.

Variable $\boldsymbol{\phi_{ctrl}}[k] = \begin{bmatrix}\phi_1^{ctrl}[k] & \phi_2^{ctrl}[k] & \dots & \phi_N^{ctrl}\end{bmatrix}^{\mathrm{T}}$ is an $N \times 1$ vector containing the outputs of the N NCOs. For the sake of the design simplicity, $\boldsymbol{\phi_{ctrl}}[k]$ is defined as an $N \times 1$ vector, but the element corresponding to the reference beam is zero. The election of the reference beam is described in section B.

A. PI CONTROLLER DESIGN

The following equation describes the system response of the j-th PI Controller:

$$G[z] = \begin{cases} G_{FLL}[z] & \sigma_{\phi_e} < \gamma \\ G_{PLL}[z] & \sigma_{\phi_e} \geq \gamma \end{cases}, \tag{13}$$

where $G_{FLL}[z]$ and $G_{PLL}[z]$ are the system responses for the 'coarse' and 'fine' synchronization steps, respectively. The parameter γ is the threshold to enable the 'fine' synchronization, and it is related to the lock-in bandwidth of $G_{PLL}[z]$. Both system responses can be designed independently [39], as discussed in the following sections.

1) Frequency synchronization

The 'coarse' or frequency synchronization step can be described as a first-order frequency-locked loop (FLL). Fig. 7 represents the main components of a digital FLL as described in [39]. As previously described, the Frequency Detector is implemented as a maximum likelihood phase detector plus an integrator. Besides, there is the first-order Loop Filter with gain K_0, an Integrator, and the NCO as a Frequency Controller [39]. The operation of the FLL can be described by its closed-loop frequency response represented in (14).

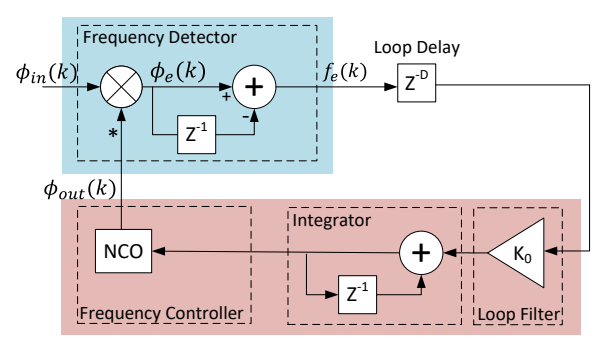

FIGURE 7. **Differential phase-error compensation loop. First state: frequency compensation.**

$$G_{FLL}[z] = \frac{\phi_{out}[z]}{\phi_{in}[z]} = \frac{K_0 z}{z^D(z-1) - K_0 z}, \tag{14}$$

where K_0 is the loop gain, and D is a natural number representing the loop delay in samples. Considering that the

This work is licensed under a Creative Commons Attribution 4.0 License. For more information, see https://creativecommons.org/licenses/by/4.0/

This article has been accepted for publication in IEEE Open Journal of the Communications Society. This is the author's version which has not been fully edited and content may change prior to final publication. Citation information: DOI 10.1109/OJCOMS.2023.3341621

compensation loop works with the estimations obtained from the non-precoded pilots, D is calculated as the ratio between the round-trip delay τ (considering that the UTs-GW loop is closed through the satellite) and the pilots' repetition interval T_p.

Considering the stability criterion for digital PLLs with loop delays [39], the loop gain K_0 must satisfy (15) to guarantee the FLL stability. Fig. 8 shows the maximum delay allowed before the loop becomes unstable for a range of loop gains $K, \quad 10^{-6} < K < 1$,

$$0 < K_0 < 2\sin\left(\frac{\pi}{2(2D+1)}\right). \tag{15}$$

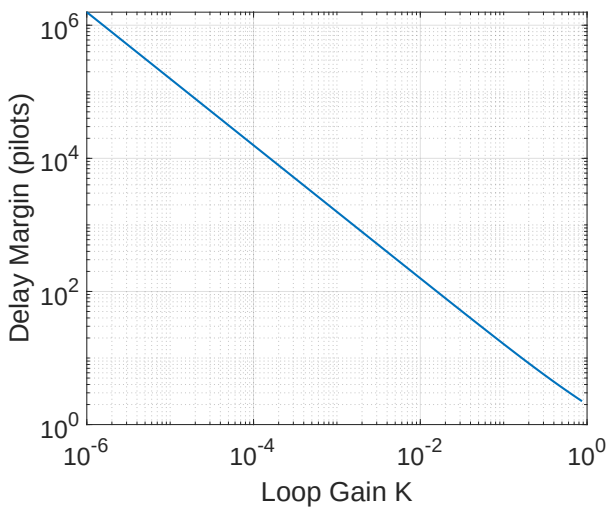

FIGURE 8. Maximum delay allowed to guarantee the stability of the compensation loop during the first state: frequency compensation.

We can calculate the maximum loop delay by knowing the satellite orbit and the UT position. For the GEO case, where the maximum slant range is around 41 127 km, $D = 3731$, which leads to a loop gain $K \leq 4 \cdot 10^{-4}$. The FLL with loop gain $K_0 = 4 \cdot 10^{-4}$ will remain stable for any delay $D \leq 3731$ pilots. Figure 9 shows the error response of the resultant frequency synchronization loop.

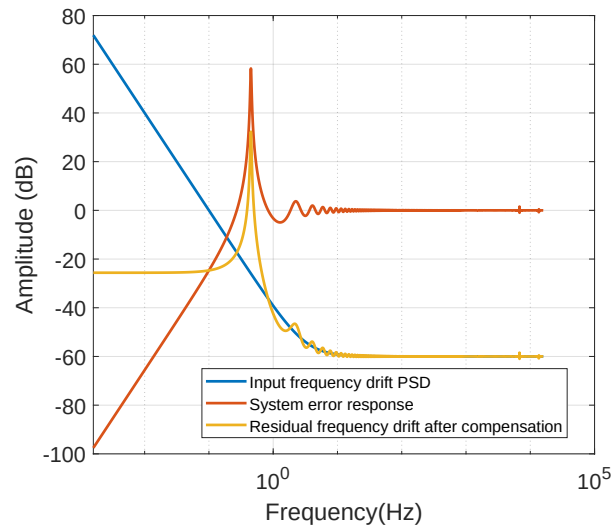

FIGURE 9. System error response of the frequency compensation loop with gain $K = 4 \cdot 10^4$

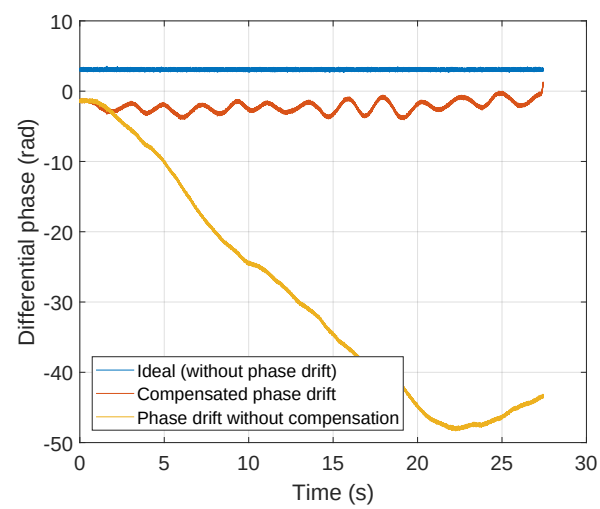

FIGURE 10. Comparison of the phase drift of one beam in a 4x4 GEO multibeam satellite system with and without the frequency compensation loop ($K = 4 \cdot 10^4$).

2) Phase synchronization

The 'fine' or phase synchronization step is based on a second-order PLL. In this case, the system response is [40]

$$G_{PLL}[z] = \frac{K_{P1}z + (K_{I1} - K_{P1})}{z^{D+1} - 2z^D + z^{z-1} + K_{P1}z + (K_{I1} - K_{P1})} \tag{16}$$

where K_{P1} and K_{I1} are the filter loop's proportional and integral gains, and D is the loop delay in samples.

The design of the 'fine' synchronization step is strongly related to the transfer function of the system $G_p[z]$, also known as the forward-path transfer function. Fig. 11 represents a simplification of the diagram in Fig. 6, where $G_c[z] = K_{P1} + \frac{K_{I1}}{1-z^{-1}}$ is the transfer function of the PI controller. For the 'coarse' synchronization state, the transfer function $G_p[z]$ contains the response of the NCO and the loop delay in pilots D, $G_p[z] = \frac{z^{-D}}{1-z^{-1}}$.

The PI controller was designed following the frequency-domain design described in [41]. This procedure calculates the values of K_{P1} and K_{I1} considering the desired phase margin (PM) of the compensated system. The PM is a parameter closely linked to the system's stability. It is defined in [41] as the amount of pure phase delay that can be added before the system becomes unstable.

Theoretically, a system is stable if the PM of the open-loop transfer function of the compensated system is in the interval

This work is licensed under a Creative Commons Attribution 4.0 License. For more information, see https://creativecommons.org/licenses/by/4.0/

This article has been accepted for publication in IEEE Open Journal of the Communications Society. This is the author's version which has not been fully edited and content may change prior to final publication. Citation information: DOI 10.1109/OJCOMS.2023.3341621

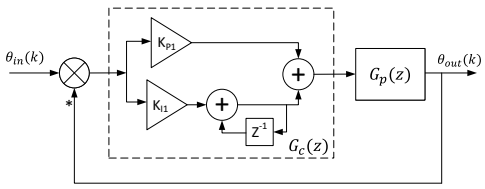

FIGURE 11. Frequency domain PI Controller design

$0 \leq$ PM $\leq 90°$. Meanwhile, practical implementations aim for a PM between $45°$ and $60°$ [42]. However, the exact value is left to the designer's discretion. Figure 12 shows the parameters of the PI controller obtained with the frequency-domain design method mentioned above. To generate the figure, we used as input the interval $0 \leq$ PM $\leq 90°$.

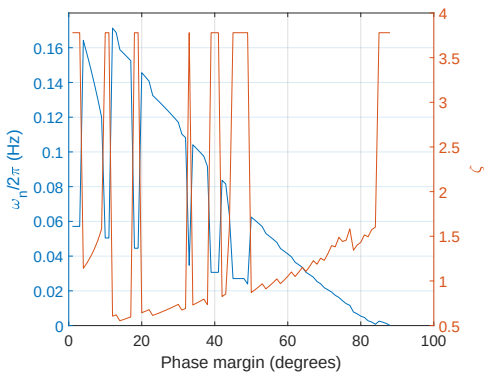

FIGURE 12. Design of the phase compensation loop as a second-order PLL. Values of ω_n (left y-axis) and ζ (right y-axis) for the PM of the open-loop transfer function in the interval $0 \leq$ PM $\leq 90°$

The left axis in Fig. 12 represents the natural frequency of the second-order loop $\omega_n = \frac{\sqrt{K_{I1}}}{2\pi T_p}$ while the right axis represents the damping factor $\zeta = \frac{K_{P1}}{2\sqrt{K_{I1}}}$. We select these parameters to exploit the similarities of the second step of our compensation loop with a classical second-order PLL. Additionally, the natural frequency and damping factor parameters offer a more intuitive description of the closed-loop system response. For instance, the natural frequency is directly related to the loop bandwidth, which makes it inversely proportional to the residual phase drift after compensation. This implies that a high value of ω_n is desired to decrease the residual phase drift. Additionally, it is well known that the damping factor of second-order PLLs should be in the interval $0.7 \leq \zeta \leq 1.5$ to guarantee stability. Considering these design criteria, we selected $\omega_n = 0.102$ Hz and $\zeta = 0.751$ for a PM = 35°. Fig. 13 shows the error response of the system for these parameters.

Similarly to Fig. 8 for the FLL, we obtained the delay margin of the system for the set of parameters 10^{-2} Hz $\leq \omega_n \leq 100$ Hz and $\zeta \in \{0.5, 0.75, 1, 1.5\}$. This is represented in Fig. 14. This figure suggests that the maximum delay allowed before the loop becomes unstable for the selected

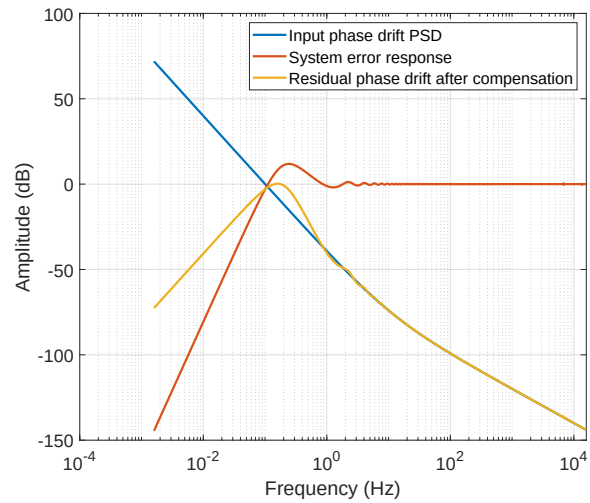

FIGURE 13. System error response of the phase compensation loop designed for an open-loop PM = 35° ($\omega_n = 0.102$ Hz; $\zeta = 0.751$)

parameters ($\omega_n = 0.102$ Hz; $\zeta = 0.751$) is higher than the previously considered $D = 3731$ pilots.

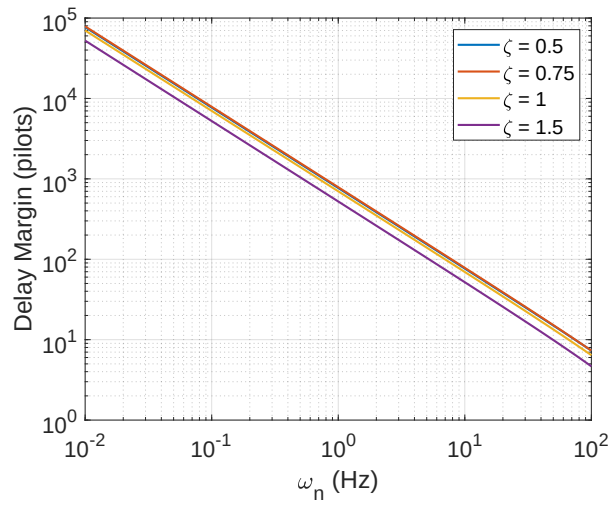

FIGURE 14. Maximum delay allowed to guarantee the stability of the compensation loop during the second state: phase compensation

Fig. 15 shows the PM of the open-loop system response with parameters ($\omega_n = 0.102$ Hz; $\zeta = 0.751$) for a loop delay in the interval $100 < D < 9000$. As mentioned before, for loops delays below the value used for the design D the system remains stable. However, this is not always the case when the loop delay is higher than the value considered for the design ($D = 3731$). The gray zone in Fig. 14 represents the loop delay values for which the system is unstable $D \geq 7700$ pilots.

Figure 16 is an example of the phase drift of one beam in a 4x4 GEO multibeam satellite system with and without the compensation loop ($\omega_n = 0.102$ Hz; $\zeta = 0.751$). In this

This work is licensed under a Creative Commons Attribution 4.0 License. For more information, see https://creativecommons.org/licenses/by/4.0/

This article has been accepted for publication in IEEE Open Journal of the Communications Society. This is the author's version which has not been fully edited and content may change prior to final publication. Citation information: DOI 10.1109/OJCOMS.2023.3341621

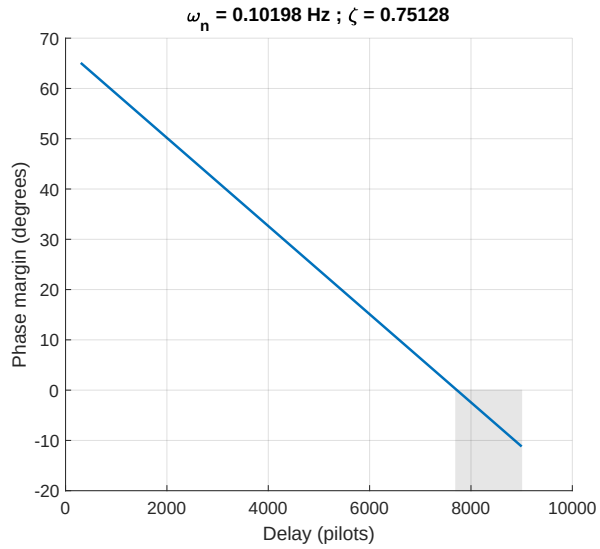

FIGURE 15. Phase Margin of the open-loop system response with parameters ($\omega_n = 0.102$ Hz; $\zeta = 0.751$) when the actual delay of the loop is in the interval $100 \leq D \leq 9000$ pilots. The grey zone represents the values of loop delay that make the loop unstable.

figure, the yellow line represents the drift in the phase of the estimated CSI when the compensation loop is not enabled, the red curve is the phase of the estimated CSI with the compensation loop, and the blue line represents the ideal scenario where there is no phase drift. This simulation was run in Matlab for a symbol rate $Rs = 6.5$ Msps.

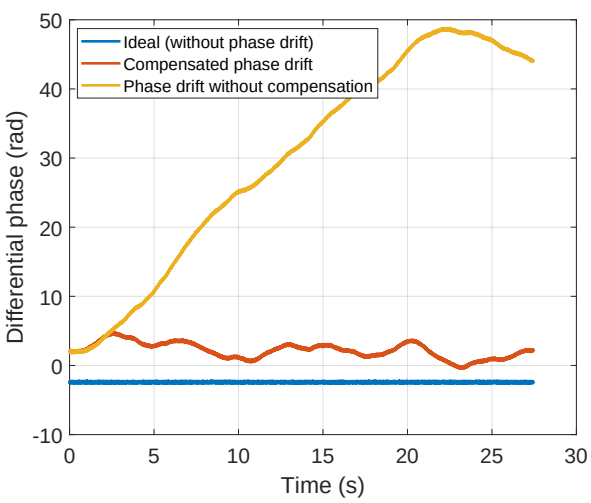

FIGURE 16. Comparison of the phase drift of one beam in a 4x4 GEO multibeam satellite system with and without the phase compensation loop ($\omega_n = 0.102$ Hz; $\zeta = 0.751$).

B. COMBINE ESTIMATIONS METHODS

As part of normal precoding o DVB-S2X operations, the UTs send to the GW their estimated thermal noise σ_i^2, with $i \in \{1, 2, ..., K\}$. Using these measurements, and the estimated CSI's amplitude $|\hat{\boldsymbol{H}}[k]|$ we can define a $K \times N$ matrix $\boldsymbol{\Gamma}$ as:

$$\boldsymbol{\Gamma} = \boldsymbol{\Sigma}|\hat{\boldsymbol{H}}[k]|^2 = \begin{bmatrix} \frac{|\hat{h}_{11}[k]|^2}{\sigma_1^2} & \frac{|\hat{h}_{12}[k]|^2}{\sigma_1^2} & \dots & \frac{|\hat{h}_{1N}[k]|^2}{\sigma_1^2} \\ \frac{|\hat{h}_{21}[k]|^2}{\sigma_2^2} & \frac{|\hat{h}_{22}[k]|^2}{\sigma_2^2} & \dots & \frac{|\hat{h}_{2N}[k]|^2}{\sigma_2^2} \\ \vdots & \vdots & \ddots & \vdots \\ \frac{|\hat{h}_{K1}[k]|^2}{\sigma_K^2} & \frac{|\hat{h}_{K2}[k]|^2}{\sigma_K^2} & \dots & \frac{|\hat{h}_{KN}[k]|^2}{\sigma_K^2} \end{bmatrix}, \tag{17}$$

where $\boldsymbol{\Sigma} = \text{diag}\left(\frac{1}{\sigma_1^2}, \frac{1}{\sigma_2^2}, ..., \frac{1}{\sigma_K^2}\right)$ is a diagonal matrix containing the thermal noise estimation from each UT.

From now on, we will refer to $\boldsymbol{\Gamma}$ as the Weight matrix since we use it as a metric for the accuracy of the interference measurement in $\boldsymbol{\Theta}[k]$ and $\boldsymbol{F}[k]$. For the sake of clarity, we rewrite both matrices as (18) and (19) below.

It is essential to notice that the elements in $\boldsymbol{\Theta}[k]$ are phase measurements with intrinsic estimation errors. Then, the Combine Estimates block's objective is to provide the most accurate differential phase and frequency estimation vectors $\boldsymbol{\theta}[k]$ and $\boldsymbol{f}[k]$ with respect to a reference beam. The resultant combined phase vector $\boldsymbol{\theta}[k]$ can be expressed as $\boldsymbol{\theta}[k] = [C_1 + (\phi_1^e[k] - \phi_{RB}^e[k]) \quad \dots \quad 0 \quad \dots \quad C_N + (\phi_N^e[k] - \phi_{RB}^e[k])]$, where $C_j \in (-\pi, \pi]$ for all $j \in \{1, 2, ..., N\}$ are constants related to the channel phase rotation $\boldsymbol{\Psi}$. Meanwhile, $C_j \approx 0$ for all $j \in \{1, 2, ..., N\}$ in the resultant combined frequency vector $\boldsymbol{f}[k]$.

For the explanation of the estimates combination, we will consider as input the matrix $\boldsymbol{F}[k]$ and as output the vector $\boldsymbol{f}$, as it is represented in Fig. 17. The main reason for this selection is that the derivative operation attenuates the effect of $\boldsymbol{\Psi}$ in $\boldsymbol{F}[k]$ matrix since $C_j \approx 0$. Consequently, combinatorial approaches such as Equal-gains combining and Weighted averages are feasible, which is not the case when using $\boldsymbol{\Theta}[k]$ as input.

There are two main groups of possible ways to combine phase measurements: by selection or by combination. The first case refers to the approaches that select the "best" measurement and discard the rest. In contrast, the second case intends to combine the measurements of a unique physical process obtained from different estimators. Among the most popular combinatorial measurement approaches, we can find Equal-gains combining and Weighted averages. However, in this article, we will analyze only the last one since its superiority has been extensible proven. In addition, we will discuss the basic approach and two other selective approaches.

1) Basic approach

This implies using the estimations from the UT with less thermal noise,

$$(i, j) = \text{argmax}\{\boldsymbol{\Sigma}\}. \tag{20}$$

This work is licensed under a Creative Commons Attribution 4.0 License. For more information, see https://creativecommons.org/licenses/by/4.0/

This article has been accepted for publication in IEEE Open Journal of the Communications Society. This is the author's version which has not been fully edited and content may change prior to final publication. Citation information: DOI 10.1109/OJCOMS.2023.3341621

$$\begin{aligned}\boldsymbol{\Theta}[k] &= \begin{bmatrix} 0 & \theta_{12}[k] & \dots & \theta_{1N}[k] \\ \theta_{21}[k] & 0 & \dots & \theta_{2N}[k] \\ \vdots & \vdots & \ddots & \vdots \\ \theta_{K1}[k] & \theta_{K2}[k] & \dots & \theta_{KN}[k] \end{bmatrix} \\ &= \begin{bmatrix} 0 & \dots & \psi_{1N} + \phi_N^e[k] - \psi_{11} - \phi_1^e[k] \\ \psi_{21} + \phi_1^e[k] - \psi_{22} - \phi_2^e[k] & \dots & \psi_{2N} + \phi_N^e[k] - \psi_{22} - \phi_2^e[k] \\ \vdots & \ddots & \vdots \\ \psi_{K1} + \phi_1^e[k] - \psi_{KK} - \phi_K^e[k] & \dots & \psi_{KN} + \phi_N^e[k] - \psi_{KK} - \phi_K^e[k] \end{bmatrix}\end{aligned} \tag{18}$$

$$\begin{aligned}\boldsymbol{F}[k] &= \boldsymbol{\Theta}[k] - \boldsymbol{\Theta}[k-1] \\ &= \begin{bmatrix} 0 & \dots & \phi_N^e[k] - \phi_1^e[k] - \phi_N^e[k-1] + \phi_1^e[k-1] \\ \phi_1^e[k] - \phi_2^e[k] - \phi_1^e[k-1] + \phi_2^e[k-1] & \dots & \phi_N^e[k] - \phi_2^e[k] - \phi_N^e[k-1] + \phi_2^e[k-1] \\ \vdots & \ddots & \vdots \\ \phi_1^e[k] - \phi_K^e[k] - \phi_1^e[k-1] + \phi_K^e[k-1] & \dots & \phi_N^e[k] - \phi_K^e[k] - \phi_N^e[k-1] + \phi_K^e[k-1] \end{bmatrix}\end{aligned} \tag{19}$$

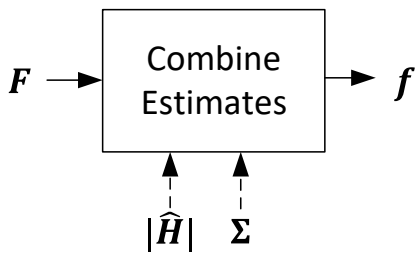

FIGURE 17. **Combine estimates block**

Since $\boldsymbol{\Sigma}$ is a diagonal matrix, $i = j$

$$\boldsymbol{f} = \boldsymbol{F}(i, :), \tag{21}$$

and the Reference beam is the i-th UT intended beam. Note that this approach does not consider the CSI's amplitude matrix $|\hat{\boldsymbol{H}}[k]|$.

2) Best receiver approach

The second approach considers that depending on their geographical location, the UTs receives the interference beams with different power. This implies that more accurate estimations can be obtained from the UT that receives more power for the higher number of beams. The goal of this approach is to select that UT and use its phase measurements for the compensation loop.

First, we calculate the "total weight" for each UT as $q_k = \sum_{n=1}^{N} \left(\frac{|\hat{h}_{kn}[k]|^2}{\sigma_k^2} \right)$, where $\frac{|\hat{h}_{kn}[k]|^2}{\sigma_k^2}$ are the elements of matrix $\boldsymbol{\Gamma}$. In a vector form $\boldsymbol{q} = \begin{bmatrix} q_1 & \dots & q_k & \dots & q_K \end{bmatrix}$ is a vector that contains a metric of the quality of the UTs. Notice that this approach requires making zero the main diagonal of $\boldsymbol{\Gamma}$ to remove the influence of the intended beam.

Then, the reference beam is the intended beam for the receiver $i = \text{argmax}\{\boldsymbol{q}\}$ and the output vector is

$$\boldsymbol{f} = \boldsymbol{F}(i, :). \tag{22}$$

The Best receiver approach is very similar to the Basic approach since all the measurements are obtained from a single UT. However, as can be seen in 18, choosing a different UT can improve the accuracy of the phase estimations. Another interesting fact about this approach is that it is possible to know in advance which may be the "Best receiver" by knowing the UTs' location and the footprint of the beams.

3) Best estimation approach

The Best estimation approach explores the idea that there is no need to use the measurements from only one UT. The phase difference between two beams is estimated in the intended receiver of each of them. Then, the Best estimation approach compares the weight of both estimations to select the more accurate measurement.

The algorithm takes two input arguments: the estimated CFO $\boldsymbol{F}$ and the Weight matrix $\boldsymbol{\Gamma}$. Basically, it iterates over each beam (j) and UT (i) pair to calculate the weights and select the best estimates. This loop performs the following steps:

- Check Conditions: The algorithm compares the weights of the current pair of estimations ($\boldsymbol{\Gamma}(i, j)$ and $\boldsymbol{\Gamma}(j, i)$. If $\boldsymbol{\Gamma}(i, j)$ is greater, it selects the weight and value of the ith UT measurement, ($\boldsymbol{\Gamma}(i, j)$ and $\boldsymbol{F}(i, j)$). Otherwise, it selects the weight and the negated phase value of the jth UT measurement ($\boldsymbol{\Gamma}(j, i)$ and $-1\boldsymbol{F}(i, j)$).
- Update the recorded Weight and Phase arrays: The algorithm updates the *weight* and phBestEst arrays with the selected weight and phase values.

Then, the algorithm identifies the reference beam by summing the weights for each beam in *weight* and selecting the one with the maximum sum. Finally, it selects in phBestEst the measurements relative to the reference beam. The pseudocode for this algorithm is shown in Algorithm 1.

This work is licensed under a Creative Commons Attribution 4.0 License. For more information, see https://creativecommons.org/licenses/by/4.0/

This article has been accepted for publication in IEEE Open Journal of the Communications Society. This is the author's version which has not been fully edited and content may change prior to final publication. Citation information: DOI 10.1109/OJCOMS.2023.3341621

Algorithm 1 Best estimation algorithm

```
procedure BESTEST(F, Γ)
    [Nu, Nt] ← size(F)
    for j = 1 : Nt do
        for i = 1 : Nu do
            if j ≠ i then
                if Γ(j,i) > Γ(i,j) then
                    weight(j,i) ← Γ(j,i)
                    phBestEst(j,i) ← F(j,i)
                else
                    weight(j,i) ← Γ(i,j)
                    phBestEst(j,i) ← −1 ∗ F(i,j)
                end if
            end if
        end for
    end for
    rowSum ← sum(weight)                ▷ Sum by row
    refBeam ← index(max(rowSum))
    combinedEst ← wrapToPi(phBestEst(refBeam))
    return (combinedEst, refBeam)
end procedure
```

4) Weighted average approach

The Weighted average approach combines all the measurements from all the UTs using the values in $\boldsymbol{\Gamma}$ as weights. This method selects as RB the beam received by the highest number of UTs. Formally, the beam $i = \text{argmax}\{\boldsymbol{q}\}$ is the RB, where $\boldsymbol{q}$ is a $1 \times N$ vector of elements

$$q_n = \sum_{k=1}^{K} \left\{ \frac{|\hat{h}_{kn}[k]|^2}{\sigma_k^2} \right\}. \tag{23}$$

The elements $f_n,\ n \in \{1, ..., N\}$ of the resultant frequency estimation vector $\boldsymbol{f}$ are calculated as follows:

$$f_n = \sum_{k=1}^{K} \left(\frac{\gamma_{kn}}{\sum_{k=1}^{K} \gamma_{kn}} \left(F(k,n) - F(k,RB) \right) \right), \tag{24}$$

where $\gamma_{kn} = \sqrt{\frac{|\hat{h}_{kRB}|^2 |\hat{h}_{kn}|^2}{\sigma_k^2 (|\hat{h}_{kRB}|^2 + |\hat{h}_{kn}|^2)}}$ is a metric for the accuracy of the differential estimation between beams n and RB measured at the k-th UT. It is worth noting that γ_{kn} is obtained as a combination of the weights $\frac{|\hat{h}_{kn}[k]|^2}{\sigma_k^2}$ and $\frac{|\hat{h}_{kRB}[k]|^2}{\sigma_k^2}$ from (17) for the measurements $F(k,n)$ and $F(k,RB)$ respectively.

5) Comparison of the combination approaches

Figure 18 represents the mean absolute error (MAE) of the different combination approaches. The MAE is calculated as the average of the absolute difference between the actual value α, and the result of the combination $\hat{\alpha}_i$, as it is described in (25),

$$MAE = 20 \log \left(\frac{1}{N} \sum_{i=1}^{N} |\alpha - \hat{\alpha}_i| \right). \tag{25}$$

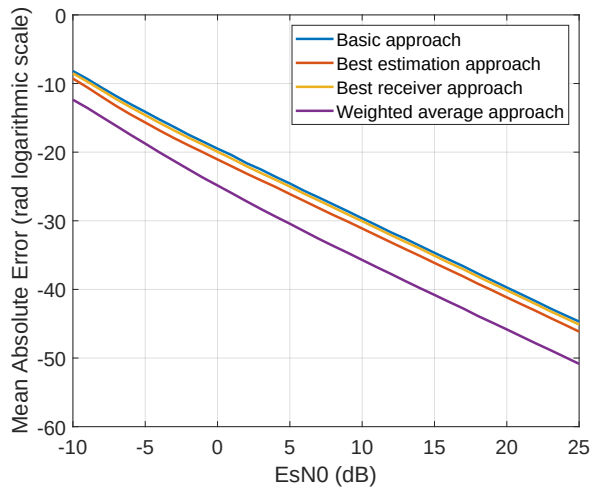

FIGURE 18. **Frequency combination**

The curves in Fig. 18 were generated by Monte Carlo simulations of the phase drift estimation and combination in a 4×4 system. The objective of our experiment is to compare the accuracy of the combination approaches described before. To that end, a phase drift vector $\boldsymbol{\alpha}$ was added to the pilots and transmitted through a randomly generated channel. At the UTs, the CSI's phase estimates were combined using the four approaches to calculate the MAE of each of them. The experiments were run for a set of energy per bit to noise power spectral density ratio $EsN0 \in \{-10, ..., 25\}$. This parameter only refers to the intended beam and doesn't consider the interference power.

The phase drift vector $\boldsymbol{\alpha} = \begin{bmatrix} \alpha_1 & ... & \alpha_4 \end{bmatrix}^{\mathrm{T}}$ had four independent elements α_n uniformly distributed with values $\alpha_n \in (-\pi; \pi)$. The transmitted pilots were predefined orthogonal Walsh-Hadamard sequences of 32 BPSK-modulated symbols, and the channel matrix was independently generated for each simulation as a 4×4 complex random matrix. The UTs performed the correlation between the received signal and the expected Walsh-Hadamard sequences to obtain the CSI estimation. Then, we calculated the frequency drift between consecutive pilots using (12) and applied the combination approaches described before. The MAE between the resultant vectors after combination $\hat{\boldsymbol{\alpha}}$, and the original phase drift $\boldsymbol{\alpha}$ were averaged over 10 thousand independent iterations and represented in Fig. 18.

As illustrated in Fig. 18, all the combination approaches considering (17) outperform the Basic approach with a constant ratio over the $EsN0$ set of values. Numerically, the accuracy improvement of each approach with respect to the basic one is: 4.4% for the Best estimation approach, 1.2%

This work is licensed under a Creative Commons Attribution 4.0 License. For more information, see https://creativecommons.org/licenses/by/4.0/

This article has been accepted for publication in IEEE Open Journal of the Communications Society. This is the author's version which has not been fully edited and content may change prior to final publication. Citation information: DOI 10.1109/OJCOMS.2023.3341621

for the Best receiver approach and 17.5% for the Weighted average approach.

IV. HARDWARE TEST-BED IMPLEMENTATION

For the experimental validation, we employ the in-house developed MIMO end-to-end satellite emulator based on SDR platforms. The proposed architecture consists of a multichannel GW with precoding capabilities, a MIMO satellite channel emulator (ChEm), a set of independent UTs, and a return-link emulator.

In general terms, the demonstrator can be described as follows. The GW subsystem generates the data packets according to the extension of the Digital Video Broadcasting - Satellite second generation (DVB-S2X) standard, using Superframe Format II structure, and applies the selected precoding method: zero-forcing (ZF), MMSE, or MMSE per-antenna power-constrained (MMSE PAC). The ChEm replicates the whole forward link chain, from the intermediate frequency (IF) input of the gateway block up-converter, toward the low-noise block down-converter IF output at the UT. It emulates the impairments present in the GW, the payload, the downlink channel, and the UTs. The UT subsystems implement the synchronization and decoding features in the DVB-S2X compliant receivers and perform the CSI estimation. Finally, the return-link emulator allows each UT to send its estimated CSI to the GW.

The GW, ChEm, and UT subsystems are being implemented using a set of SDR platforms, specifically the USRP-2944R from National Instruments, as depicted in Fig. 19. The physical interfaces of the channel emulator with the gateway and the user terminals are provided by the interconnection of the 50-Ω ports of the SDRs, employing IF modulated signals. The SDR platforms in the GW and the ChEm are synchronized with the same clock reference. This eliminates any timing misalignment due to their LOs, allowing precise control of the time mismatch according to the implemented impairment models.

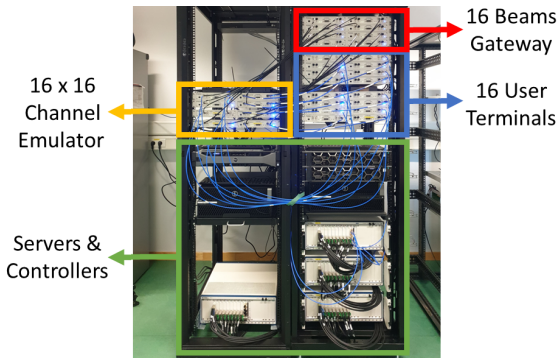

FIGURE 19. SDR-based MIMO end-to-end satellite emulator.

All system components have been successfully tested considering a GEO satellite scenario [31], [43], [44]. This includes the use of implementations of the GW and UTs subsystems in the precoding validation over a live GEO link [31]. The test-bed is upgraded by including the two-state phase noise model at the ChEm and the PI controller and combine estimations blocks at the GW. The following subsections will describe the implementation of these blocks.

1) TWO-STATE PHASE NOISE MODEL IMPLEMENTATION

Figure 20 represents the block diagram of the two-state model hardware implementation. The model requires as input two independent zero-mean Gaussian random vectors with unitary variance, $p_1[k]$ and $p_2[k]$. Inputs σ_1 and σ_2 represent the standard deviation of $p_1[k]$ and $p_2[k]$ respectively.

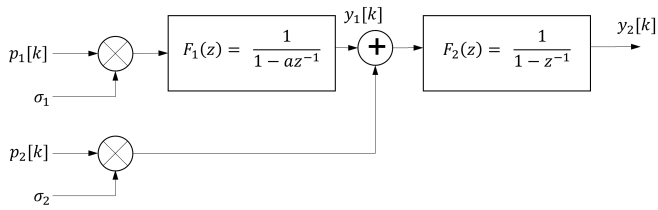

FIGURE 20. Block diagram of the Two-state model implementation

The diagram in Fig. 20 was implemented as an intellectual property block using Vivado HLS. Figure 21 shows the hardware implementation of the Phase Noise Generator block. In the figure, the two pseudo-random generators provide $p_1[k]$ and $p_2[k]$, and the values of sigma_1 (σ_1) and sigma_2 (σ_2) are defined at the user interface. The inputs sigma_1 and sigma_2 are obtained from the desired phase noise mask using algorithm 2.

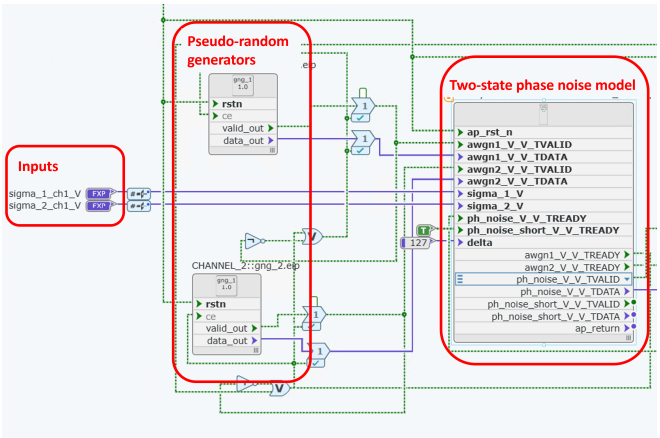

FIGURE 21. Hardware implementation of the two-state model

The target phase noise mask, in logarithmic scale, can be described by the parameters: h_{-2} for the -20 dB/dec slope and h_{-4} for the -40 dB/dec slope:

$$S_\phi(f) = 10\log\left(\frac{h_{-4}}{f^4} + \frac{h_{-2}}{f^2}\right). \tag{26}$$

Additionally, the PSD obtained from the two-state model can be described by the coordinate pair $(f_\phi; A_\phi)$ where both regions ($\alpha = 4$ and $\alpha = 2$) intercept. Hereafter this point

This work is licensed under a Creative Commons Attribution 4.0 License. For more information, see https://creativecommons.org/licenses/by/4.0/

This article has been accepted for publication in IEEE Open Journal of the Communications Society. This is the author's version which has not been fully edited and content may change prior to final publication. Citation information: DOI 10.1109/OJCOMS.2023.3341621

Algorithm 2 Calculate variance algorithm

procedure VAR_CALC(A_ϕ, f_ϕ, f_s)
  $h_4 \leftarrow 10^{A_\phi/10} * (2\pi f_\phi)^4$
  $h_2 \leftarrow 10^{A_\phi/10} * (2\pi f_\phi)^2$
  $q_1 \leftarrow h_2/2$
  $q_2 \leftarrow 2\pi^2 h_4$
  $\sigma_1 \leftarrow q_1/f_s + q_2/(3f_s^3)$
  $\sigma_2 \leftarrow q_2/f_s$
  return (σ_1, σ_2)
end procedure

$(f_\phi; A_\phi)$ will be used to identify the phase noise masks. For instance, (10 Hz; -75 dBc/Hz) refers to the two-state PSD with a -40 dB/dec slope region for $f < 10$ Hz and -20 dB/dec slope region for $f > 10$ Hz; $S_\phi(10) = -75$ dBc/Hz as shown in Fig. 3.

The Phase Noise Generator block was integrated with the MIMO end-to-end satellite emulator presented in [45] as part of the ChEm's universal software radio peripherals (USRP). This allows including the phase noise for the LOs in the uplink and the downlink independently.

2) PI CONTROLLER IMPLEMENTATION

The PI controller was implemented as an intellectual property block using Vivado HLS. Figure 22 shows the resultant block in LABVIEW. As can be appreciated, it has two main inputs: *gamma* and *fed*. The first one is an array with the values of the proportional K_P and integral K_I gains. The second input, *fed*, is the differential frequency or phase used to calculate the output *fnco*, which is the compensation phase calculated by the PI controller. Four block instances were connected in the GW's USRP, where the compensation calculated by the PI controller is applied to the superframe data streams by NCO-mixer blocks.

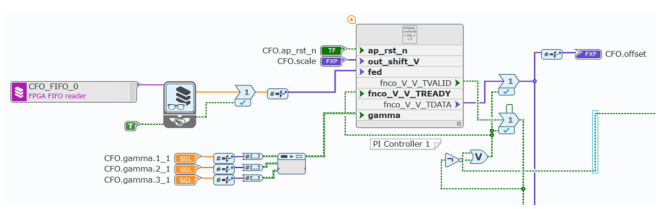

FIGURE 22. PI controller block

3) COMBINE ESTIMATIONS IMPLEMENTATION

The Combine Estimations block was implemented as a switch-case structure in the GW's Host PC. A drop-down menu at the user interface shown in Fig. 24 allows selecting the desired approach. Table 1 represents the naming equivalence between the user interface in Fig. 24 and the rest of this article. We added the option of manually setting the reference beam in addition to the previously described methods: basic approach, best receiver, best estimation, and weighted average. Due to their simplicity, the Basic approach and the Best Receiver methods were implemented using LABVIEW's blocks. However, for the Best Estimation and the Weighted Average cases, the Interface for MATLAB functionality allowed us to run the MATLAB functions from LABVIEW. Fig. 23 shows the implementation of the Best Receiver Combine estimation approach. In this figure, the inputs are represented in orange, while the outputs are in green.

TABLE 1. Combine Estimations's user interface naming equivalence

	Parameter	Name in Fig. 24
Input Matrices	CFO ($\boldsymbol{F}[k]$)	est_CFO
	differential phase ($\boldsymbol{\Theta}[k]$)	est_DiffPhase
Weights	amplitude of the CSI ($\lvert\hat{\boldsymbol{H}}[k]\rvert^2$)	Weight Matrix
	UTs' noise variance $[\sigma_1^2, \sigma_2^2, ..., \sigma_K^2]$	Noise_var
Output Vectors	CFO ($\boldsymbol{f}[k]$)	Combined CFO
	differential phase ($\boldsymbol{\theta}[k]$)	Combined DiffPhase

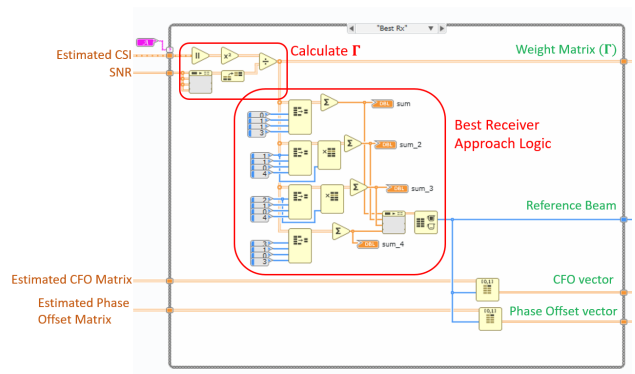

FIGURE 23. Combine estimations: Best Receiver approach implementation

To validate the hardware implementation of this block, we showcase the input matrices $\boldsymbol{F}[k]$ and $\boldsymbol{\Theta}[k]$, as well as the output vectors $\boldsymbol{f}[k]$ and $\boldsymbol{\theta}[k]$, in the graphic user interface (see Fig. 24). The user interface also presents the amplitude of the CSI estimation $|\hat{\boldsymbol{H}}[k]|^2$ and the noise variance measured by the UTs. Using these displayed parameters, the Combine Estimations algorithm computes the Weight matrix as defined in (17). Subsequently, we calculate the resultant vectors for each input matrix across all proposed approaches. For instance, Fig. 24 shows one example using the Basic approach. In this case, the UT with less noise is the UT 2 since the minimum value of the UT's noise variance is 0.008099. As can be seen in the figure, the output differential phase vector $[119.371, 61.865, 0, -86.0963]$ and the output carrier frequency offset (CFO) vector $[0.081097, 13.4486, 0, 0.212494]$ are the third row of the corresponding input matrices. Notably, the results obtained using the hardware block, the Matlab algorithm, and our calculations align consistently in all instances.

This work is licensed under a Creative Commons Attribution 4.0 License. For more information, see https://creativecommons.org/licenses/by/4.0/

This article has been accepted for publication in IEEE Open Journal of the Communications Society. This is the author's version which has not been fully edited and content may change prior to final publication. Citation information: DOI 10.1109/OJCOMS.2023.3341621

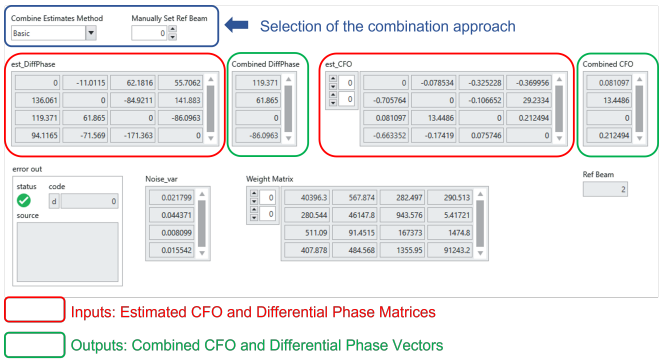

FIGURE 24. Combine estimations: Graphic user interface to select the combination approach.

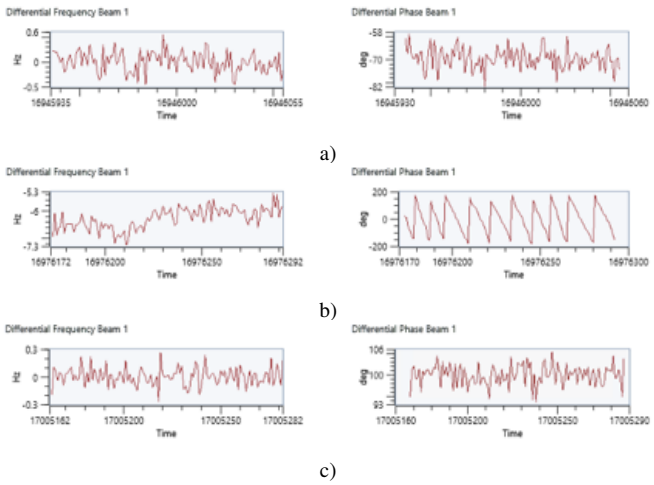

FIGURE 25. Frequency and phase drift with LOs phase noise at the uplink and downlink: a) Ideal case without LOs' phase noise, b) Phase noise only in the uplink, c) Phase noise only in the downlink.

V. EXPERIMENTAL PERFORMANCE EVALUATION

In this section, we evaluate the impact of the phase noise and the proposed solution on the performance of a multibeam satellite system. To that end, we set the MIMO end-to-end satellite test-bed to emulate a 4×4 precoding-enabled GEO satellite system.

As a first experiment, we set the phase noise mask (-75 dBc/Hz @ 10 Hz) in Fig. 3 for the LOs in the uplink and the downlink independently. Fig. 25 shows the differential frequency and phase for beam 1 measured at the UT 0. These are the differential frequency and phase measurements between beams 0 and 1. In the figure, we included the ideal case, where the LOs do not have phase noise, as a comparison baseline. Note that unlike the downlink case (c)), the phase noise in the uplink channel (b)) does affect the system performance.

The second experiment was designed to validate the design of the phase compensation loop. In this case, we set the phase noise mask (10 Hz; -75 dBc/Hz) in the uplink and analyzed the differential frequency and phase between beams 0 and 1 measured at UT 0. The results of this experiment are shown in Fig. 26. As can be appreciated in the figure, the first state

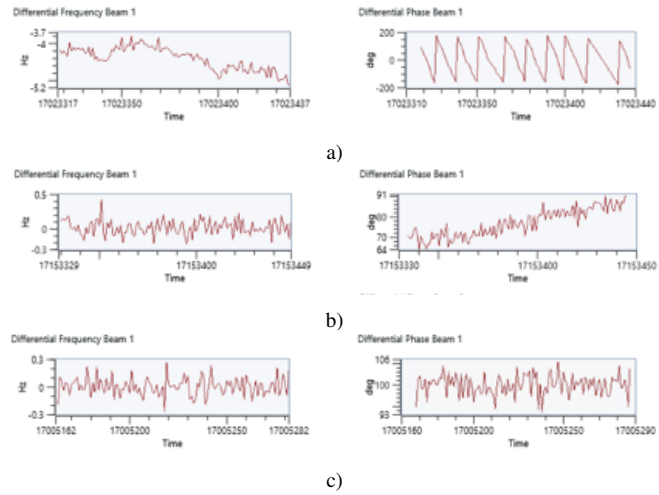

FIGURE 26. Frequency and phase drift during the phase synchronization: a) Phase noise in the uplink channel, phase compensation loop disabled, b) Phase compensation loop enabled, working in the first state (frequency synchronization), phase noise only in the uplink channel, c) Phase compensation loop enabled, working in the second state (phase synchronization), phase noise only in the uplink channel.

of the proposed compensation loop reduces the frequency drift below 1 Hz. However, this is insufficient to keep the differential phase stable, see Fig. 26 b). Finally, the differential phase is compensated when the phase synchronization state is enabled Fig. 26 c).

In addition, Fig. 27 illustrates the impact of the compensation loop on system performance. Specifically, the received symbols and signal-to-noise-plus-interference ratio (SNIR) of UT 1 are presented with and without precoding for two scenarios: a) when the compensation loop is disabled and b) when enabled. As depicted in Fig. 27a, disabling the compensation loop results in no increase in received SNIR with the precoding technique. However, in Fig. 27b, with the compensation loop enabled, the precoding technique significantly enhances the received SNIR by at least 10 dB.

These experiments highlight the main contributions of our article: the proposed synchronization algorithm, or an equivalent, is essential for practical implementations of the precoding techniques. Without synchronizing the phases of the transmitted beams, the performance benefits promised by precoding techniques remain unattainable. The primary challenge in implementing our solution in multibeam satellite systems lies in the need for periodic feedback from the UTs to the GW. While this requirement is also present in implementing precoding, our solution demands more data and more frequent feedback than traditional precoding methods. A potential resolution to this challenge could involve selecting which UTs should report their phase estimations, considering the combine estimation approaches discussed in this article.

This work is licensed under a Creative Commons Attribution 4.0 License. For more information, see https://creativecommons.org/licenses/by/4.0/

This article has been accepted for publication in IEEE Open Journal of the Communications Society. This is the author's version which has not been fully edited and content may change prior to final publication. Citation information: DOI 10.1109/OJCOMS.2023.3341621

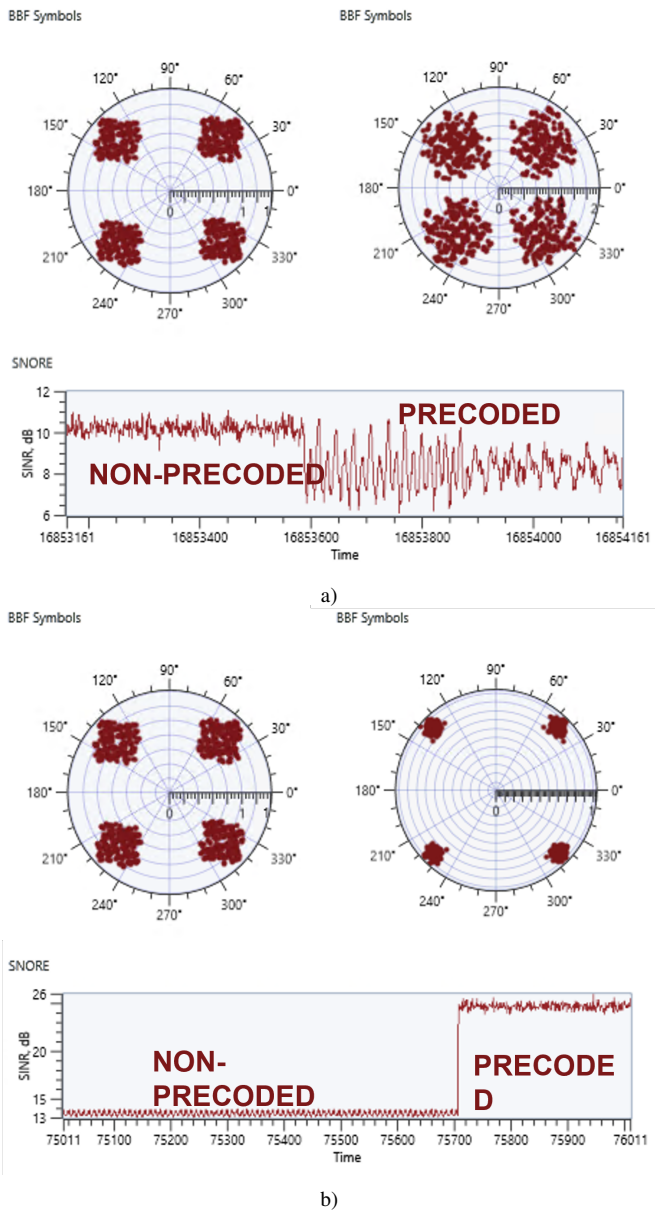

FIGURE 27. received symbols and UT's SNIR: a) with the compensation loop disabled, b)with the compensation loop enabled.

VI. CONCLUSIONS

This article contains the design and implementation of the phase compensation loop required to enable the precoding technique in GEO scenarios. One key strength of the proposed solution is its simplicity, requiring only small modifications to the previously considered precoding implementations—specifically, incorporating a phase compensation loop at the GW. The compensation loop proposed in this article is based on PI controllers, widely used in industrial control systems for their proven effectiveness.

Moreover, the article introduces various approaches for combining the phase and frequency measurements from the UTs and assesses their performance using Matlab simulations. The choice of the combine estimates algorithm is expected to influence the practical implementation of the proposed synchronization algorithm, potentially reducing the amount of feedback data needed for the compensation loop. Subsequent research should extensively investigate the trade-offs among achievable accuracy, algorithm complexity, and the volume of feedback data for the combined estimation methods. Additionally, it is worth noting that the combination approaches explored in this article represent straightforward and well-known cases. Future research may explore more complex algorithms such as the methods used in multisensor data fusion [25]–[29].

The hardware implementation of the compensation loop and the combination of phase measurements were described, along with the implementation of the two-state phase noise model. These blocks were integrated into the in-house developed MIMO end-to-end satellite emulator based on SDR platforms to validate the proposed closed-loop synchronization method's performance. The hardware experimentation validates the viability of the proposed solution for real-world scenarios. The primary challenge in implementing this solution within an actual multibeam satellite system lies in the periodic transmission of measurements from the UTs to the GW. Moreover, this work can be extended by considering other combinatorial approaches for the Combine Estimations block. In this regard, exploring methods proposed for multisensor data fusion in wireless sensor networks could be beneficial.

In summary, the successful implementation of our phase compensation loop, grounded in PI controllers, demonstrates the proposed solution's simplicity and adaptability and underscores its robust performance in real-world scenarios. The comprehensive validation through hardware experimentation and integration into the MIMO satellite emulator showcases the practical effectiveness of our closed-loop synchronization method, paving the way for enhanced GEO multibeam satellite systems.

REFERENCES

[1] Z. Lin, K. An, H. Niu, Y. Hu, S. Chatzinotas, G. Zheng, and J. Wang, "SLNR-Based Secure Energy Efficient Beamforming in Multibeam Satellite Systems," *IEEE Transactions on Aerospace and Electronic Systems*, vol. 59, no. 2, pp. 2085–2088, 2023.

[2] M. A. Vazquez, A. Perez-Neira, D. Christopoulos, S. Chatzinotas, B. Ottersten, P.-D. Arapoglou, A. Ginesi, and G. Tarocco, "Precoding in Multibeam Satellite Communications: Present and Future Challenges," *IEEE Wireless Communications*, vol. 23, no. December, pp. 88–95, 2016.

[3] V. Joroughi, M. Vazquez, and A. I. Perez-Neira, "Generalized multicast multibeam precoding for satellite communications," *IEEE Transactions on Wireless Communications*, vol. 16, no. 2, pp. 952–966, 2017.

[4] E. Lagunas, A. Pérez-Neira, M. Martínez, M. A. Lagunas, M. A. Vázquez, and B. Ottersten, "Precoding With Received-Interference Power Control for Multibeam Satellite Communication Systems," *Frontiers in Space Technologies*, vol. 2, no. May, pp. 1–12, 2021.

[5] M. A. Albreem, A. H. A. Habbash, A. M. Abu-Hudrouss, and S. S. Ikki, "Overview of precoding techniques for massive mimo," *IEEE Access*, vol. 9, pp. 60 764–60 801, 2021.

[6] O. Haliloglu, J. Sadreddini, and P. Frenger, "Interference-aware distributed precoding in coherent large-scale distributed mimo," in *2021 IEEE Globecom Workshops (GC Wkshps)*, 2021, pp. 1–6.

This work is licensed under a Creative Commons Attribution 4.0 License. For more information, see https://creativecommons.org/licenses/by/4.0/

This article has been accepted for publication in IEEE Open Journal of the Communications Society. This is the author's version which has not been fully edited and content may change prior to final publication. Citation information: DOI 10.1109/OJCOMS.2023.3341621

[7] O. Kodheli, E. Lagunas, N. Maturo, S. K. Sharma, B. Shankar, J. F. M. Montoya, J. C. M. Duncan, D. Spano, S. Chatzinotas, S. Kisseleff, J. Querol, L. Lei, T. X. Vu, and G. Goussetis, "Satellite Communications in the New Space Era: A Survey and Future Challenges," *IEEE Communications Surveys & Tutorials*, pp. 1–45, 2020. [Online]. Available: http://arxiv.org/abs/2002.08811

[8] L. M. Marrero, J. C. M. Duncan, J. Querol, S. Chatzinotas, A. Camps, and B. Ottersten, "A design strategy for phase synchronization in Precoding-enabled DVB-S2X user terminals," *IEEE International Conference on Communications*, 2021.

[9] P. Savazzi and A. Vizziello, "Carrier synchronization in distributed mimo satellite links," in *2015 IEEE International Conference on Wireless for Space and Extreme Environments (WiSEE)*, 2015, pp. 1–6.

[10] G. Jin, R. Wang, K. Liu, D. Liu, D. Liang, H. Zhang, N. Ou, Y. Zhang, Y. Deng, and C. Li, "An Advanced Phase Synchronization Scheme for LT-1," *IEEE Transactions on Geoscience and Remote Sensing*, vol. 58, no. 3, pp. 1735–1746, 2020.

[11] L. Belostotski, T. Landecker, and D. Routledge, "A technique for microwave ranging and remote phase synchronization," *IEEE Transactions on Instrumentation and Measurement*, vol. 51, no. 3, pp. 551–559, jun 2002. [Online]. Available: http://ieeexplore.ieee.org/document/1017727/

[12] H. Yan, S. Hanna, K. Balke, R. Gupta, and D. Cabric, "Software Defined Radio Implementation of Carrier and Timing Synchronization for Distributed Arrays," in *2019 IEEE Aerospace Conference*, nov 2018. [Online]. Available: http://arxiv.org/abs/1811.02098

[13] L. M. Marrero, A. Haqiqatnejad, J. C. M. Duncan, S. Chatzinotas, and B. Ottersten, "Multiuser-MISO Precoding under Channel Phase Uncertainty in Satellite Communication Systems," *IEEE Open Journal of Vehicular Technology*, vol. PP, pp. 1–21, 2022.

[14] J. Rutman, "Characterization of Phase and Frequency Instabilities in Precision Frequency Sources: Fifteen Years of Progress." *Proceedings of the IEEE*, vol. 66, no. 9, pp. 1048–1075, 1978.

[15] A. Gharanjik, M. R. Bhavani Shankar, P. D. Arapoglou, M. Bengtsson, and B. Ottersten, "Robust precoding design for multibeam downlink satellite channel with phase uncertainty," in *ICASSP, IEEE International Conference on Acoustics, Speech and Signal Processing - Proceedings*, vol. 2015-Augus, 2015, pp. 3083–3087.

[16] G. Taricco, "Linear Precoding Methods for Multi-Beam Broadband Satellite Systems," in *European Wireless 2014; 20th European Wireless Conference; Proceedings of*, 2014, pp. 1–6.

[17] Mubarak Umar Aminu, J. Lehtomäki, and Markku Juntti, "Beamforming and Transceiver Optimization with Phase Noise for mmWave and THz Bands," in *16th International Symposium on Wireless Communication Systems ISWCS 2019*, Oulu, Finland, 2019.

[18] A. Chorti and M. Brookes, "A spectral model for RF oscillators with power-law phase noise," *IEEE Transactions on Circuits and Systems I: Regular Papers*, vol. 53, no. 9, pp. 1989–1999, 2006.

[19] J. Mcneill, S. Razavi, K. Vedula, and D. Richard, "Experimental Characterization and Modeling of Low-Cost Oscillators for Improved Carrier Phase Synchronization," in *2017 IEEE International Instrumentation and Measurement Technology Conference (I2MTC)*, Turin, Italy, 2017. [Online]. Available: http://spinlab.wpi.edu/pubs/McNeill_I2MCT_2017.pdf

[20] L. Galleani, "A tutorial on the two-state model of the atomic clock noise," *Metrologia*, vol. 45, no. 6, 2008.

[21] F. Lavancier and P. Rochet, "A general procedure to combine estimators," *Computational Statistics and Data Analysis*, vol. 94, pp. 175–192, 2016. [Online]. Available: http://dx.doi.org/10.1016/j.csda.2015.08.001

[22] H. Liu, S. Fang, and J. Jianhua, "An improved weighted fusion algorithm of multi-sensor," *Journal of Physics: Conference Series*, 2019.

[23] T. Yücek and H. Arslan, "A survey of spectrum sensing algorithms for cognitive radio applications," *IEEE Communications Surveys and Tutorials*, vol. 11, no. 1, pp. 116–130, 2009.

[24] C. M. Dharmapuri and B. V. Reddy, "Performance Analysis of Different Fusion Rules for Cooperative Spectrum Sensing in Cognitive Radio Communication," in *Proceedings of the 17th INDIACom; 2023 10th International Conference on Computing for Sustainable Global Development, INDIACom 2023*. Bharati Vidyapeeth, New Delhi, 2023, pp. 1061–1064.

[25] Y. Zhang, A. Xiong, Y. Xiao, and Z. Chen, "A new combination method based on pearson coefficient and information entropy for multi-sensor data fusion," *Information and Software Technology*, vol. 161, p. 107248, 2023. [Online]. Available: https://www.sciencedirect.com/science/article/pii/S0950584923001027

[26] M. K. Al-Sharman, B. J. Emran, M. A. Jaradat, H. Najjaran, R. Al-Husari, and Y. Zweiri, "Precision landing using an adaptive fuzzy multi-sensor data fusion architecture," *Applied Soft Computing*, vol. 69, pp. 149–164, 2018. [Online]. Available: https://www.sciencedirect.com/science/article/pii/S1568494618302163

[27] L. A. Zadeh, "A note on z-numbers," *Information Sciences*, vol. 181, no. 14, pp. 2923–2932, 2011. [Online]. Available: https://www.sciencedirect.com/science/article/pii/S0020025511001046

[28] Y. Deng, "D numbers: theory and applications," *Journal of Information &Computational Science*, vol. 9, no. 9, pp. 2421–2428, 2012.

[29] Y. Tian, X. Mi, L. Liu, and B. Kang, "A new soft likelihood function based on d numbers in handling uncertain information," *International Journal of Fuzzy Systems*, vol. 22, no. 7, pp. 2333–2349, 2020.

[30] K. U. Storek, R. T. Schwarz, and A. Knopp, "Multi-satellite multi-user MIMO precoding: Testbed and field trial," in *IEEE International Conference on Communications (ICC)*, June, 2020, pp. 1–7.

[31] J. Krivochiza, J. C. M. Duncan, J. Querol, N. Maturo, L. M. Marrero, S. Andrenacci, J. Krause, and S. Chatzinotas, "End-to-end precoding validation over a live GEO satellite forward link," *IEEE Access*, vol. 4, pp. 1–10, 2021.

[32] M. Li and M. Diao, "Cooperative spectrum sensing algorithm based on majority decision fusion," in *Proceedings of the 2012 2nd International Conference on Instrumentation and Measurement, Computer, Communication and Control, IMCCC 2012*, no. 1. IEEE, 2012, pp. 952–956.

[33] R. Agarwal, N. Srivastava, and H. Katiyar, "Energy detection of unknown signals over Rayleigh fading channel for EGC and SSC diversity combining techniques," in *International Conference on Emerging Trends in Electrical, Electronics and Sustainable Energy Systems, ICETEESES 2016*. IEEE, 2016, pp. 116–119.

[34] A. P. Theeksha and S. Srikanth, "Performance analysis and mode selection of su-mimo and mu-mimo in 802.11ac," in *2013 International Conference on Recent Trends in Information Technology (ICRTIT)*, 2013, pp. 732–737.

[35] D. M. Pozar, *Microwave engineering*, 4th ed. Danvers, MA: John Wiley & Sons, 2012.

[36] I. Standards, *IEEE Std 1139-2008 (Revision of IEEE Std 1139-1999) IEEE Standard Definitions of Physical Quantities for Fundamental Frequency and Time Metrology–Random Instabilities*, 2009, vol. 2008, no. February.

[37] J. A. McNeill and D. S. Ricketts, *The Designer's Guide to Jitter in Ring Oscillators*. Springer, 2009, no. 1.

[38] C. Zucca and P. Tavella, "The clock model and its relationship with the Allan and related variances," *IEEE Transactions on Ultrasonics, Ferroelectrics and Frequency Control*, vol. 52, no. 2, pp. 289–296, feb 2005. [Online]. Available: http://ieeexplore.ieee.org/document/1406554/

[39] Fuyun Ling, "Digital Frequency-Locked Loop," in *Synchronization in Digital Communication Systems*. Cambridge University Press, 2017, ch. Carrier Sy, pp. 193–270.

[40] U. Mengali and A. N. D'Andrea, *Synchronization techniques for digital receivers*, ser. Applications of communications theory 1075407. New York: Plenum Press, 1997.

[41] F. Golnaraghi, *Design of Control Systems*. New York: Wiley, 2010.

[42] J. Bergmans, "Effect of loop delay on phase margin of first-order and second-order control loops," *IEEE Transactions on Circuits and Systems II: Express Briefs*, vol. 52, no. 10, pp. 621–625, 2005.

[43] J. Duncan, J. Krivochiza, S. Andrenacci, S. Chatzinotas, and B. Ottersten, "Hardware demonstration of precoded communications in multibeam UHTS systems," in *36th International Communications Satellite Systems Conference (ICSSC 2018)*, 2018, pp. 1–5.

[44] N. Maturo, J. C. M. Duncan, J. Krivochiza, J. Querol, D. Spano, S. Chatzinotas, and B. Ottersten, "Demonstrator of precoding technique for a multi-beams satellite system," in *2019 8th International Workshop on Tracking, Telemetry and Command Systems for Space Applications (TTC)*, 2019, pp. 1–8.

[45] J. Duncan, J. Querol, N. Maturo, J. Krivochiza, D. Spano, N. Saba, L. Marrero, S. Chatzinotas, and B. Ottersten, "Hardware precoding demonstration in multibeam UHTS communications under realistic payload characteristics," in *ICSSC2019*, vol. 2019, no. CP774, 2019.

This work is licensed under a Creative Commons Attribution 4.0 License. For more information, see https://creativecommons.org/licenses/by/4.0/

This article has been accepted for publication in IEEE Open Journal of the Communications Society. This is the author's version which has not been fully edited and content may change prior to final publication. Citation information: DOI 10.1109/OJCOMS.2023.3341621

Liz Martinez Marrero(S'18-M'23) was born in Havana, Cuba, in 1989. She received the M.Sc. degree in telecommunications and Telematics from the Technological University of Havana (CUJAE), Cuba, in 2018. She is currently working toward the Ph.D. degree as a Doctoral Researcher at the Interdisciplinary Centre for Security, Reliability, and Trust (SnT) of the University of Luxembourg. Her research interests include digital signal processing for wireless communications, focusing on the physical layer, satellite communications, and carrier synchronization for distributed systems.

During the 37th International Communications Satellite Systems Conference (ICSSC2019) she received the Best Student Paper Award.

Juan Carlos Merlano Duncan(S'09-M'12) received the Diploma degree in electrical engineering from the Universidad del Norte, Barranquilla, Colombia, in 2004, the M.Sc. and Ph.D. Diploma (Cum Laude) degrees from the Universitat Politècnica de Catalunya (UPC), Barcelona, Spain, in 2009 and 2012, respectively. His research interests are wireless communications, remote sensing, distributed systems, frequency distribution and carrier synchronization systems, software-defined radios, and embedded systems.

At UPC, he was responsible for the design and implementation of a radar system known as SABRINA, which was the first ground-based bistatic radar receiver using space-borne platforms, such as ERS-2, ENVISAT, and TerraSAR-X as opportunity transmitters (C and X bands). He was also in charge of the implementation of a ground-based array of transmitters, which was able to monitor land subsidence with subwavelength precision. These two implementations involved FPGA design, embedded programming, and analog RF/Microwave design. In 2013, he joined the Institute National de la Recherche Scientifique, Montreal, Canada, as a Research Assistant in the design and implementation of cognitive radio networks employing software development and FPGA programming. He joined the University of Luxembourg since 2016, where he currently works as a Research Scientist in the COMMLAB laboratory working on SDR implementation of satellite and terrestrial communication systems and passive remote sensing systems.

Jorge Luis González(S'09-M'18) is with the Interdisciplinary Centre for Security, Reliability and Trust (SnT), University of Luxembourg. He received his B.S. Degree (with honors), M.S. Degree and Ph.D. on Telecommunications and Electronics in 2006, 2009 and 2018, respectively, from the Technological University of Havana (CUJAE), Cuba. From September 2006 to July 2019 he was as Lecturer and Researcher with the Research Center on Microelectronics (CIME) at CUJAE. He visited the Seville Institute of Microelectronics (IMSE-CNM), Spain, in 2010, 2011 and 2012, and the Group of Microelectronics of the Federal University of Itajuba (UNIFEI), Brazil, in 2013. His research interests include RF/analog circuits, embedded systems and wireless and satellite communications.

Jevgenij Krivochiza(S'13-M'20) received the B.Sc. and M.Sc. degrees in electronic engineering in telecommunications physics and electronics from the Faculty of Physics, Vilnius University, in 2011 and 2013, respectively. He received the Ph.D. degree in electrical engineering from the Interdisciplinary Centre for Security, Reliability, and Trust (SnT), University of Luxembourg, in 2020. Currently, he is a Research Associate at SNT, University of Luxembourg. His main research topics are coming from development for FPGA silicon, software-defined radios, digital signal processing, precoding, interference mitigation, DVB-S2X, DVB-S2, and LTE systems. He works on digital signal processor (DSP) algorithms for SDR platforms for advanced precoding and beamforming techniques in next-generation satellite communications.

Symeon Chatzinotas(S'06-M'09-SM'13-F'23) received the M.Eng. degree in telecommunications from the Aristotle University of Thessaloniki, Thessaloniki, Greece, in 2003, and the M.Sc. and Ph.D. degrees in electronic engineering from the University of Surrey, Surrey, U.K., in 2006 and 2009, respectively. He is currently a Full Professor, Chief Scientist I, and Head of the research group SIGCOM in the Interdisciplinary Centre for Security, Reliability and Trust, University of Luxembourg. In parallel, he is an Adjunct Professor in the Department of Electronic Systems at the Norwegian University of Science and Technology and a Collaborating Scholar of the Institute of Informatics & Telecommunications, National Center for Scientific Research "Demokritos."

In the past, he has lectured as Visiting Professor at the University of Parma, Italy, and contributed to numerous R&D projects for the Institute of Telematics and Informatics, Center of Research and Technology Hellas and Mobile Communications Research Group, Center of Communication Systems Research, University of Surrey.

He has authored more than 700 technical papers in refereed international journals, conferences, and scientific books. He has received numerous awards and recognitions, including the IEEE Fellowship and an IEEE Distinguished Contributions Award. He is currently on the editorial board of the IEEE Transactions on Communications, IEEE Open Journal of Vehicular Technology, and the International Journal of Satellite Communications and Networking.

Björn Ottersten(S'87–M'89–SM'99–F'04) received the M.S. degree in electrical engineering and applied physics from Linköping University, Linköping, Sweden, in 1986, and the Ph.D. degree in electrical engineering from Stanford University, Stanford, CA, USA, in 1990. He has held research positions with the Department of Electrical Engineering, Linköping University, the Information Systems Laboratory, Stanford University, the Katholieke Universiteit Leuven, Leuven, Belgium, and the University of Luxembourg, Luxembourg. From 1996 to 1997, he was the Director of Research with ArrayComm, Inc., a start-up in San Jose, CA, USA, based on his patented technology. In 1991, he was appointed Professor of signal processing with the Royal Institute of Technology (KTH), Stockholm, Sweden. Dr. Ottersten has been Head of the Department for Signals, Sensors, and Systems, KTH, and Dean of the School of Electrical Engineering, KTH. He is currently the Director for the Interdisciplinary Centre for Security, Reliability and Trust, University of Luxembourg. He is a recipient of the IEEE Signal Processing Society Technical Achievement Award, the EURASIP Group Technical Achievement Award, and the European Research Council advanced research grant twice. He has co-authored journal papers that received the IEEE Signal Processing Society Best Paper Award in 1993, 2001, 2006, 2013, and 2019, and 9 IEEE conference papers best paper awards. He has been a board member of IEEE Signal Processing Society, the Swedish Research Council and currently serves of the boards of EURASIP and the Swedish Foundation for Strategic Research. Dr. Ottersten has served as Editor in Chief of EURASIP Signal Processing, and acted on the editorial boards of IEEE Transactions on Signal Processing, IEEE Signal Processing Magazine, IEEE Open Journal for Signal Processing, EURASIP Journal of Advances in Signal Processing and Foundations and Trends in Signal Processing. He is a fellow of EURASIP.

This work is licensed under a Creative Commons Attribution 4.0 License. For more information, see https://creativecommons.org/licenses/by/4.0/

This article has been accepted for publication in IEEE Open Journal of the Communications Society. This is the author's version which has not been fully edited and content may change prior to final publication. Citation information: DOI 10.1109/OJCOMS.2023.3341621

Adriano Camps(S'91-A'97-M'00-SM'03-F'11) joined the Electromagnetics and Photonics Eng. Group, Dept. of Signal Theory and Communications, UPC, as an Assistant Professor in 1993, Associate Professor in 1997, and Full Professor since 2007. In 1999, he was on sabbatical leave at the Microwave Remote Sensing Lab., of the Univ. of Massachusetts, Amherst. His research interests are focused in: 1) microwave remote sensing, with special emphasis in microwave radiometry by aperture synthesis (PhD Thesis was about the MIRAS instrument which became the single payload of ESA's SMOS mission), 3) remote sensing using signals of opportunity (GNSS-R), 4) radio frequency interference detection and mitigation, and 5) nanosatellites as a tool to test innovative remote sensors. His publication record includes over 245 papers in peer-reviewed journals, 9 book chapters and the book Emery and Camps, "Introduction to Satellite Remote Sensing. Atmosphere, Ocean, Land and Cryosphere Applications," Elsevier, 2017, 860 pages), and more than 485 conference presentations. According to Google Scholar/Scopus his h-index is 56 / 44, and his publications have received more than 12933/8816 citations. He holds 12 patents, and has advised 27 Ph. D. Thesis students (+ 8 on-going), and more than 150 final project and M.Eng. Theses. He is the Scientific Coordinator of the CommSensLab Research Center (María de Maeztu Excellence Research unit 2016-2020) at the Dept of Signal Theory and Communications. Within CommSensLab, he co-leads the Remote Sensing Lab (https://prs.upc.edu/), and leads the UPC NanoSat Lab (https://nanosatlab.upc.edu/en). He is the PI of the first four UPC nanosatellites: 3Cat-1, 3Cat-2, 3Cat-4, and FSSCat, a tandem mission formed by two 6U CubeSats. FFSCAT is the first mission contributing to the Copernicus System based on CubeSats and it has produced for the first time using CubeSats scientific quality soil moisture, sea ice extent, concentration and thickness, and sea salinity maps in the Arctic. He has participated in all Technical Committee Programs of the International Geoscience and Remote Sensing Symposium (IGARSS) since 2000, was Chair of uCal 2001, Technical Program Committee Co-chair of IGARSS 2007, co-chair of GNSS-R '10, general co-chair of IGARSS 2020, the 6th FFSS Workshop, and is member of the organizing committee of the ESA 4th Symposium on Space Educational Activities (SSEA). He was Associate Editor of Radio Science, and the IEEE Geoscience and Remote Sensing Letters, and he is Associate Editor of the IEEE Transactions on Geoscience and Remote Sensing, and has been guest editor of several special issues. He was the President-Founder of the IEEE Geoscience and Remote Sensing Society (GRSS) Chapter at Spain, and 2017-2018 President of the IEEE Geoscience and Remote Sensing Society.

This work is licensed under a Creative Commons Attribution 4.0 License. For more information, see https://creativecommons.org/licenses/by/4.0/